MONTE CARLO SIMULATION OF OPTICAL COHERENCE TOMOGRAPHY OF MEDIA WITH ARBITRARY SPATIAL DISTRIBUTIONS

by

Siavash Malektaji

A Thesis submitted to the Faculty of Graduate Studies of

The University of Manitoba

in partial fulfilment of the requirements of the degree of

Master of Science

Department of Electrical and Computer Engineering

University of Manitoba

Winnipeg

Abstract

Optical Coherence Tomography (OCT) is a sub-surface imaging modality with growing number of applications. An accurate and practical OCT simulator could be an important tool to understand the physics underlying OCT and to design OCT systems with improved performance. All available OCT simulators are restricted to imaging planar multilayered media or non-planar multilayered media. In this work I developed a novel Monte Carlo based simulator of OCT imaging for turbid media with arbitrary spatial distributions. This simulator allows computation of both Class I diffusive reflectance, due to ballistic and quasi-ballistic scattered photons, and Class II diffusive reflectance due to multiple scattered photons. A tetrahedron-based mesh is used to model any arbitrary-shaped medium to be simulated. I have also implemented a known importance sampling method to significantly reduce computational time of simulations by up to two orders of magnitude. The simulator is verified by comparing its results to results from previously validated OCT simulators for multilayered media. I present sample simulation results for OCT imaging of non-layered media which would not have been possible with earlier simulators.

Acknowledgements

First and foremost, my deepest gratitude is to my advisor, Prof. Sherif S. Sherif. His support and guidance helped me in every step of my studies. I am deeply and forever indebted to him for giving me the opportunity to work under his guidance.

I would also like to thank Prof. Ivan T. Lima Jr. from electrical and computer engineering department of North Dakota state university for his generous support and insightful suggestions.

I would like to thank the members of my committee, Prof. Andrew Goertzen and Prof. Pradeepa Yahampath for taking time to read my thesis and their valuable comments.

I dedicate this thesis to my family; my father, my mother and my sister for their constant support and unconditional love. I love you all dearly.

Table of Contents

List of Figures

List of Tables

List of Abbreviations

ANSI	***A**merican **N**ational **S**tandards **I**nstitute*
CCD	***C**harge **C**oupled **D**evice*
CDF	***C**umulative **D**istribution **F**unction*
CUDA	***C**ompute **U**nified **D**evice **A**rchitecture*
DC	***D**irect **C**urrent*
DE	***D**iffusion **E**quation*
FPGA	***F**ield **P**rogrammable **G**ate **A**rray*
FWHM	***F**ull **W**idth at **H**alf **M**aximum*
GPU	***G**raphics **P**rocessor **U**nits*
GSL	***G**NU **S**cientific **L**ibrary*
HG	***H**enyey-**G**reenstein*
IS	***I**mportance **S**ampling*
K-M	***K**ubelka-**M**unk*
MCML	***M**onte **C**arlo Simulation of Light Transport in **M**ulti-**L**ayered Turbid Media*
MRI	***M**agnetic **R**esonance **I**maging*
NA	***N**umerical **A**perture*
OCT	***O**ptical **C**oherence **T**omography*
PDE	***P**artial **D**ifferential **E**quation*
PRNG	***P**seudo **R**andom **N**umber **G**enerator*
PSF	***P**oint **S**pread **F**unction*
RTE	***R**adiative **T**ransfer **E**quation*

SD-OCT	***S**pectral **D**omain **O**ptical **C**oherence **T**omography*
SNR	***S**ignal to **N**oise **R**atio*
SS-OCT	***S**wept **S**ource **O**ptical **C**oherence **T**omography*
TD-OCT	***T**ime **D**omain **O**ptical **C**oherence **T**omography*
TIM-OS	***T**etrahedron **B**ased **I**nhomogeneous **M**onte **C**arlo **O**ptical **S**imulator*

Chapter 1

Introduction

Optical Coherence Tomography (OCT) is establishing itself as an important non-invasive biomedical imaging technique. One of its earlier applications was as a diagnostic tool in ophthalmology, but its applications are rapidly growing in other biomedical and industrial fields [1][2][3][4][5][6]. A combination of penetration depth of about 2-3 mm [7] and resolution between 1 μm and 15 μm [8] makes OCT a unique imaging modality.

The study of the workings of OCT is typically performed using experimental case studies. A realistic and accurate simulator of OCT could be a useful tool to understand the physical process underlying OCT and to design OCT systems with improved imaging performance. However, an OCT simulator to image arbitrary shaped media is unavailable. All available OCT simulators are limited to planar layered media [9] [10] [11] [12] [13][14] or more recently to non-planar layered media [15].

Therefore, development of an advanced OCT simulator for media with arbitrary spatial distribution would be extremely useful. Such OCT simulator would be a powerful tool to facilitate the design of novel OCT systems with improved performance, e.g., increased depth of imaging.

1.1 Organization of this thesis

Developing an OCT simulator requires an understanding of the operation of OCT, in addition to understanding the optical properties of the tissue.

In chapter 2 the theory of OCT imaging and different types of it are briefly discussed.

To simulate OCT signals from turbid tissue, one needs to know the optical coefficients of this tissue. Furthermore, any OCT simulator would be based on a simulation of light propagation in turbid tissues. Therefore chapter 3 discusses modeling of the optical properties of tissue.

In chapter 4 I review previous works on Monte Carlo simulation of OCT imaging. In this chapter I also review modeling of arbitrary shaped media for the purpose of simulating light propagation in them.

In chapter 5 I present my novel OCT simulator and the implemented importance sampling method. Importance sampling is a family of techniques that are used to reduce variance of Monte Carlo based estimates of simulated physical quantities.

In chapter 6 I validate the simulator by comparing its results to previously validated OCT simulators of multilayered media. The media used for validation are a four layer medium used by Yao and Wang in [9] and a multilayer model of human skin proposed in [16]. I then present examples of OCT imaging simulations from two non-layered objects, a sphere inside a slab and a slab containing an ellipsoid and two spheres. I also analyze three important aspects of my novel OCT simulator: (1) resolution, (2) accuracy, and (3) computation time. Finally, in chapter 7 I present my conclusions and suggested future work.

1.2 Thesis research contributions

I developed a novel Monte Carlo based OCT simulator for arbitrary shaped media and implemented it in ANSI-C.

I used a tetrahedron mesh to model arbitrary shaped media as proposed in [17]. Tetrahedron meshes can model any media with arbitrary spatial distribution with any desired accuracy.

I implemented the importance sampling method introduced by Lima *et al.* to reduce the variance of Class I and Class II estimates [14]. I have validated the simulator by comparing its results to results from previously validated simulators. The novelty of this work is that it combines the use of tetrahedron based meshes to model arbitrary shaped media and the application of an advanced importance sampling method to simulate OCT imaging of arbitrary shaped media. I presented simulation results of OCT signals from two arbitrary-shaped media, which were not possible to obtain using previous OCT simulators. I analyzed the accuracy of these simulations results and demonstrated that the accuracy of the estimated Class I signal is reduced with imaging depth. I also demonstrated that using a previously implemented importance sampling method and a fixed number of photons, one could reduce the variance of Class I signal estimates by two orders of magnitude.

1.3 Publications related to this thesis

S. Malektaji, I. T. Lima, and S. S. Sherif, "Monte Carlo simulation of optical coherence tomography for turbid media with arbitrary spatial distributions.," *J. Biomed. Opt.*, vol. 19, no. 4, p. 046001, 2014.

S. Malektaji, I. T. Lima and S. S. Sherif, "Simulation of optical coherence tomography imaging of an arbitrary shaped turbid object.," In *Biomedical Optics*, Miami, FL, 2014, p. BT3A-69.

Chapter 2

Optical Coherence Tomography

Optical coherence tomography (OCT) is a noninvasive, noncontact subsurface imaging technique with numerous medical and industrial applications. The axial resolution of OCT is between $1\ \mu m$ to $15\ \mu m$, which is one to two orders of magnitude higher than ultrasound imaging [8]. However, since light is strongly scattered and absorbed in most tissues, imaging depth of OCT is restricted to $2-3\ mm$ which is considerably less than ultrasound imaging [7].

OCT has lower axial resolution than confocal microscopy which can reach $0.5\ \mu m$ [18]. However, penetration depth of confocal microscopy is typically less than $100\ \mu m$ which is much smaller than OCT [18]. Figure 2.1 illustrates the resolution and penetration depth of different biomedical imaging modalities compared to OCT.

As can be seen in Figure 2.1 OCT fills the gap between confocal microscopy and ultrasound imaging.

OCT imaging systems can be divided into time domain OCT (TD-OCT) and spectral domain OCT (SD-OCT). Both TD-OCT and SD-OCT use interferometry to measure backscattered light from an object.

In addition to being used for structural imaging, OCT has been used for functional imaging. Polarization sensitive OCT, Oximetry, differential absorption OCT and Doppler OCT are examples of functional OCT systems [19].

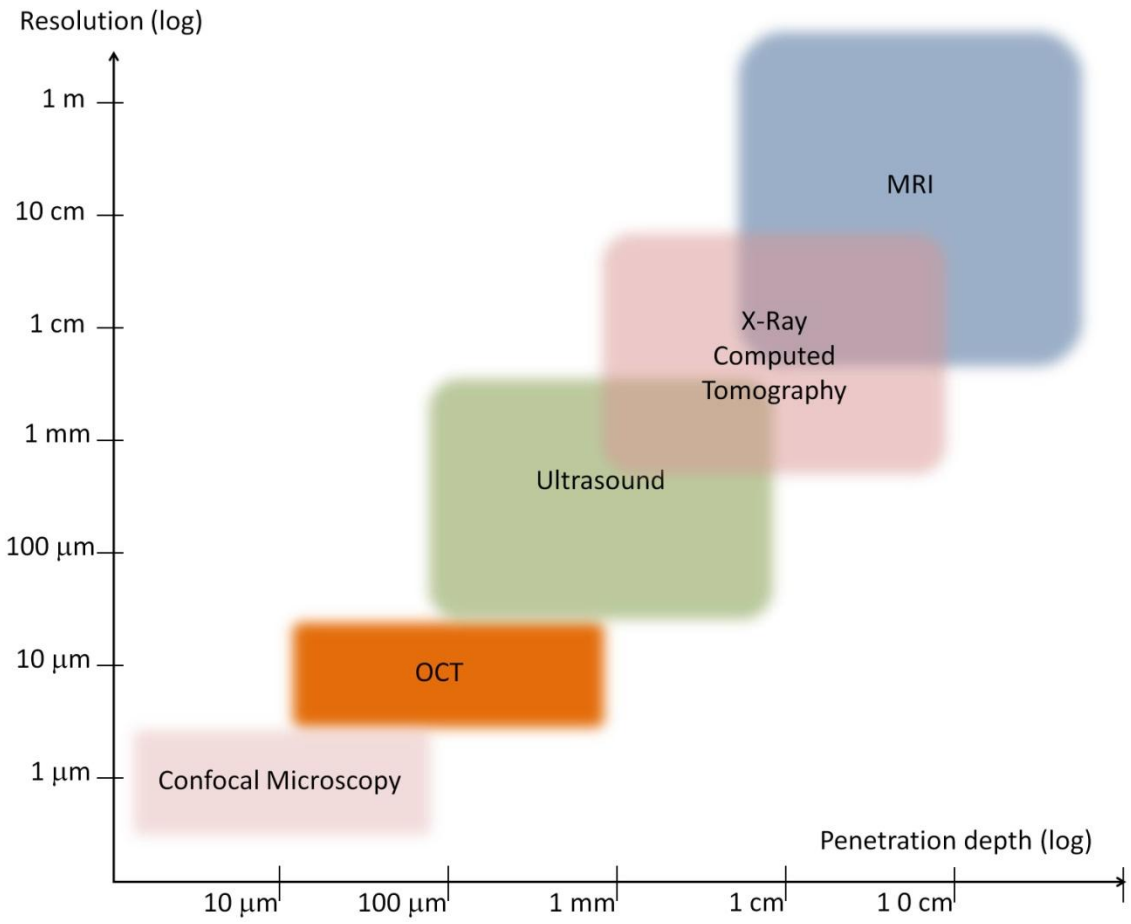

Figure 2.1 Resolution and penetration depth of different biomedical imaging modalities.

2.1 Time Domain OCT

Time domain OCT is based on low coherence interferometry. Figure 2.2 shows a schematic diagram of a Michelson interferometer used in TD-OCT. To detect the optical reflectance profile of a sample, the interference signal between the backscattered light and a known reference is measured.

Following [20] let $V_s(t)$ and $V_r(t)$ be the field at time t, in the sample arm and reference arm, respectively. The instantaneous optical power at the detector is given,

$$I_{OCT}(t) = \left| V_r[t - f(t)] + \int_0^{\infty} V_r[t - f(t)]R(\tau)d\tau \right|^2$$

$$= |V_r[t - f(t)]|^2 + \left|\int_0^\infty V_r[t - f(t)]R(\tau)d\tau\right|^2$$

$$+2Re\left\{V_r[t - f(t)]\int_0^\infty {V_r}^*[t - f(t)]R(\tau)d\tau\right\}, \tag{2.1}$$

where τ and $f(t)$ are the time delays due to propagation of light inside the sample and to the movement of the reference mirror, respectively. R is the reflectance profile of the sample. $Re\{\cdot\}$ denote the real part of a complex number. The term $\left|\int_0^\infty V_r[t - f(t)]R(\tau)d\tau\right|^2$ is typically ignored since the absolute values of R are very small [20].

The optical source is assumed to be stationary and ergodic. Therefore the statistical mean of the intensity, $E[I_{OCT}(t)]$, can be replaced with its time average, i.e.,

$$\mathrm{E}[\mathrm{I_{OCT}(t)}] \cong \langle I_{OCT}(t)\rangle, \tag{2.2}$$

where operator $\langle\cdot\rangle$ denotes time averaging. Let V_{src} be the electric field of the source. By substituting $V_r = aV_{src}$ and $V_s = bV_{src}$ in Eq. 2.1 where a and b are complex constants specific to the OCT system the statistical mean of the detected intensity is given by,

$$\mathrm{E}[\mathrm{I_{OCT}(t)}] \cong \langle|aV_{src}[t - f(t)]|^2\rangle$$

$$+ 2Re\left\{ab^*\langle V_{src}[t - f(t)] \times \int_0^\infty {V_{src}}^*[t - \tau]R(\tau)d\tau\rangle\right\}. \tag{2.3}$$

Since variations of fields $V_r(t)$ and $V_s(t)$ are considerably faster than typical photo-detectors, the statistical mean of detected intensity can be written as,

$$\mathrm{E}[\mathrm{I_{OCT}(t)}] = |a|^2\langle I_{src}\rangle + \langle I_{src}\rangle \times 2Re\left\{ab^*\int_0^\infty {\gamma_{src}}^*[f(t) - \tau]R(\tau)d\tau\right\}, \tag{2.4}$$

where γ_{src} is the autocorrelation function of the light source. If the mirror is scanned with the velocity v, i.e., $f(t) = \alpha t$, where $\alpha = \frac{2v}{c_0}$ and c_0 is the speed of light in vacuum, the statistical mean of the detected intensity would be,

$$\mathrm{E}[\mathrm{I_{OCT}(t)}] = |a|^2\langle I_{src}\rangle + \langle I_{src}\rangle \times 2Re\left\{ab^* \int_0^\infty {\gamma_{src}}^*[\alpha t - \tau]R(\tau)d\tau\right\}. \tag{2.5}$$

Typical OCT signal consists of a DC offset term and number of fringes. By measuring the positions and the magnitudes of these fringes the reflectance profile of the sample can be found.

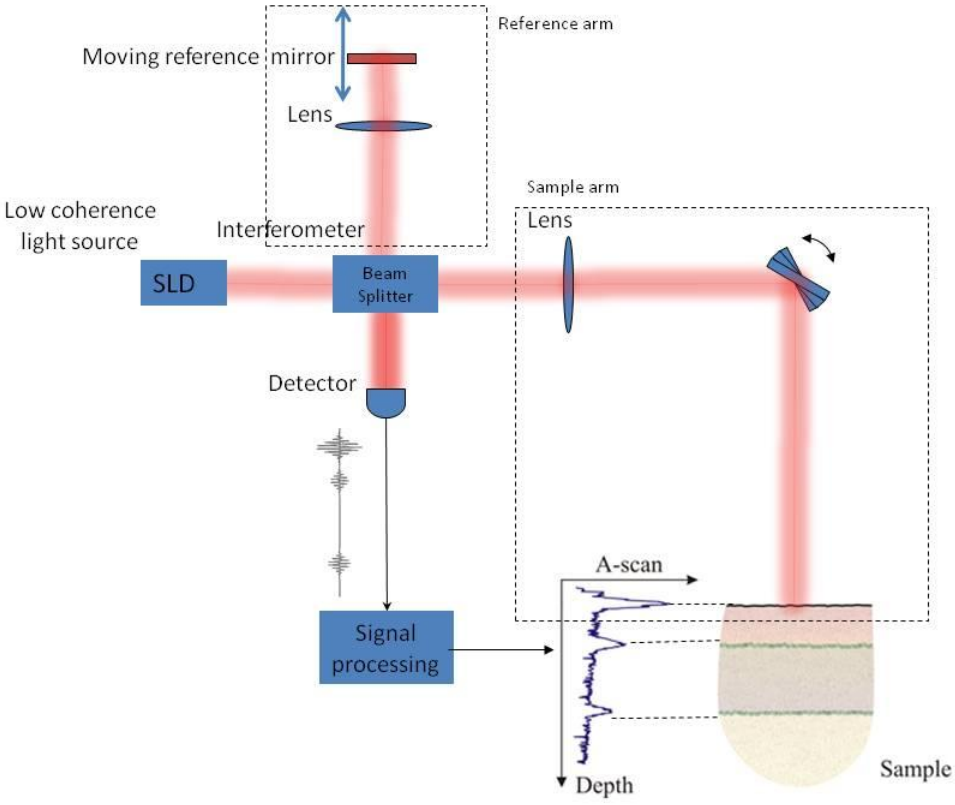

Figure 2.2 Schematic diagram of TD-OCT.

2.2 Resolution of TD-OCT

The axial resolution of the TD-OCT system depends on the coherence length of the source $l_c = c_0\tau_c$, where τ_c is the coherence time of the light source. The coherence time of the light source is the full width at half maximum (FWHM) of its autocorrelation function, γ_{src}. The spectrum of the light source is the Fourier transform of the autocorrelation function it. If source has a Gaussian spectrum, the coherence length l_c, is given by [20],

$$l_c = \frac{2\sqrt{\ln(2)}}{\Delta k} = \frac{2\ln(2)}{\pi}\frac{\lambda_0^2}{\Delta\lambda}, \tag{2.6}$$

where Δk is the spectral bandwith of the light source spectrum. $\Delta\lambda$ and λ_0 represent the wavelength bandwidth and the central wavelength of the wavelength spectrum of the light source.

The lateral resolution of OCT depends on the wavelength at the center of the spectrum of the light and numerical aperture of the finite optical beam used for imaging. If the light source is Gaussian beam, the lateral resolution of the system, δx, is given by [21],

$$\delta x = \frac{0.37\lambda_0}{NA}, \tag{2.7}$$

where NA is the numerical aperture of the optical probe in the sample arm.

2.3 Spectral Domain OCT

In Spectral-Domain OCT (SD-OCT), the mirror in the reference arm is stationary and the light source is a broadband light source as shown in Figure 2.3. SD-OCT is a tomographic approach whereas TD-OCT is localized imaging method. In this method the reflectivity profile of the sample is encoded in the different wavelength of the interference pattern. In SD-OCT sample reflectivity profile is obtained by the inverse

Fourier transform of the signal detected by a spectrometer. As shown in Figure 2.3 the spectrometer consists of a gating to separate light with different wavelengths and a CCD to detect them.

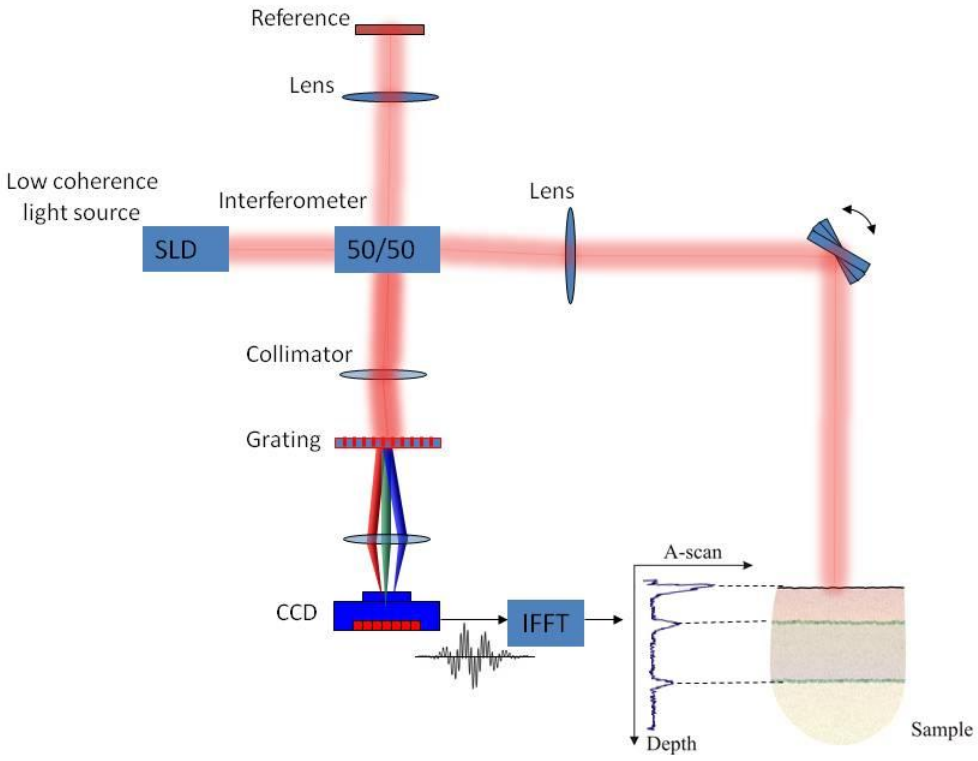

Figure 2.3 Schematic diagram of SD-OCT.

2.4 Swept Source OCT

Swept Source OCT (SS-OCT) which is also called optical frequency domain imaging (OFDI) is an alternative implementation of Spectral domain OCT. SD-OCT provides higher imaging speed than TD-OCT systems due to the simpler mechanical design of the static reference arm. It has been shown that SD-OCT typically has 20-30 dB sensitivity advantages over TD-OCT [21]. However, CCD arrays may introduce phase washout problems during the pixel integration time which cause the images to get blurred and

degraded. Also it is difficult to implement a balanced detector in the case of a 50/50 beam splitter, or possibly an unbalanced detector in other cases, to obtain a differential output. An alternative way of implementing SD-OCT, while maintaining the benefits of high-speed imaging and SNR, is SS-OCT. Figure 2.4 illustrates the schematic diagram of SS-OCT. As shown in Figure 2.4 SS-OCT uses a wavelength-tunable laser source instead of the broad band source used in SD-OCT. The output from the monochromatic light source is split between the reference arm and the sample arm. Interference between the reference beam reflected from a fixed mirror, and the light backscattered from the sample, is detected for a single wavelength at each time. The reflectivity profile of the sample is obtained by combining the measurements, obtained at different wavelengths, and performing a Fourier transform. Compared to SD-OCT, SS-OCT is relatively slower, however it still provides 50 to 100 times higher imaging speed compared to TD-OCT.

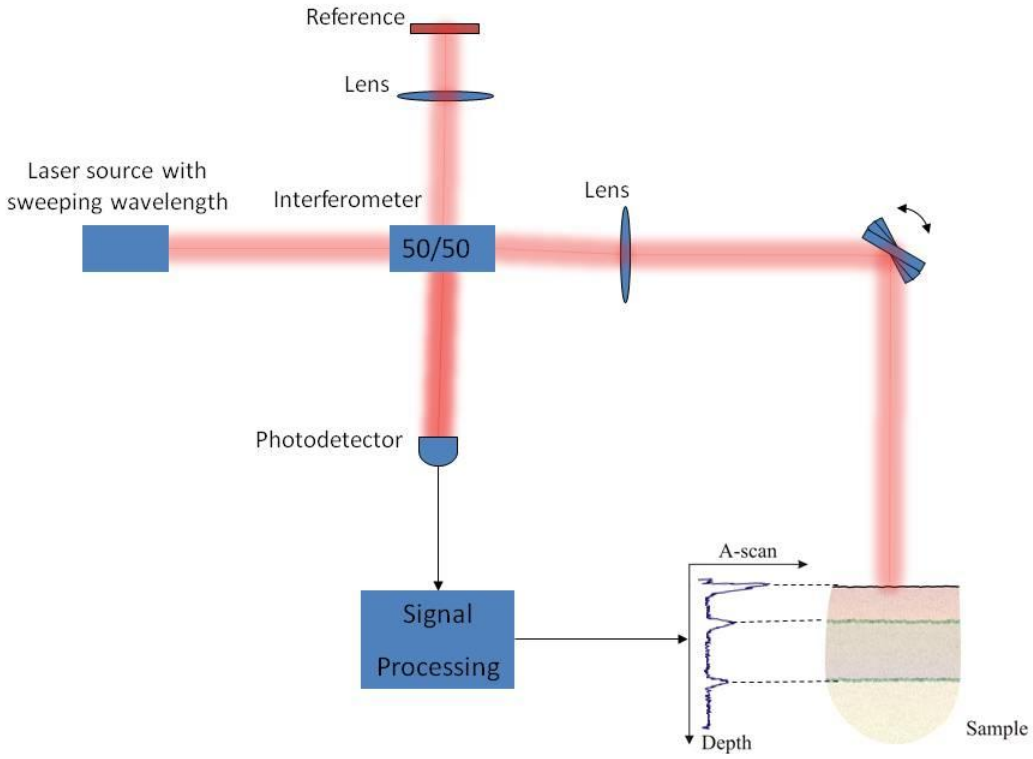

Figure 2.4 Schematic diagram of SS-OCT.

Chapter 3

Modeling Optical Properties of Tissue

Simulation of OCT signals from tissue requires its optical coefficients i.e., scattering coefficient, μ_s, absorption coefficient, μ_a, refractive index, n, and anisotropy factor g.

Two approaches can be generally used to obtain the optical coefficients of tissue: empirical measurement of such quantities or calculation form mathematical models of tissue.

Such measurements can be performed either directly or indirectly. For a direct measurement, tissue is illuminated and the percentage of light it reflects, i.e., its reflectance, or the percentage of light it transmits, i.e., its transmittance is directly measured. Afterward, estimation of the optical properties of this tissue becomes an inverse problem where these measurements are used as boundary conditions for mathematical models that describe interaction of light with tissue. For indirect measurements, thermal changes in tissue due to absorption of light are used to calculate its optical coefficients.

Different models of light propagation in tissue are described in Section 3.1, followed by a description of a particle-based model of tissue, in Section 3.2.

3.1 Theory of light transport in tissue

Two main approaches could be used to model the light transport, i.e., interaction, with tissue. One approach is based on Maxwell's equations and the other is based on the Radiative Transport Equation (RTE), also known as Boltzmann's equation. Recently it

has been shown that RTE can be derived from Maxwell's equations through proper approximations [22].

3.1.1 Radiative Transfer Equation

The RTE integro-differential equation is given by [22] [23],

$$\frac{1}{C_0}\frac{\partial}{\partial t}I(r(t),\hat{s},t) + (\mu_s+\mu_a)I(r(t),\hat{s},t) + \frac{(\mu_s+\mu_a)}{4\pi}\int_{(4\pi)} p(\hat{s}.\hat{s}')I(r(t'),\hat{s}',t)d\Omega' \qquad (3.1)$$

$$+ Q(r(t),\hat{s},t),$$

where $I(r(t),\hat{s},t)$ is the intensity at position $r(t)$, representing the amount of power per unit area that flows in the direction $\hat{s}$ at the time t [22]. $p(\hat{s}.\hat{s}')$ is the scattering phase function and $Q(r(t),\hat{s},t)$ is a source term [23]. Exact solutions of RTE are only known for restricted simple cases. Hence, RTE is usually approximated by the Diffusion Equation (DE).

3.1.2 Diffusion Equation

In the Diffusion approximation, scattering directions are assumed to be isotropic and the scattering coefficient is assumed to be considerably higher than the absorption coefficient. The DE is given by the following partial differential equation (PDE) [23]:

$$\frac{1}{C}\frac{\partial}{\partial t}\Phi_d(r(t),t) + \mu_a\Phi_d(r(t),t) - D\nabla^2\Phi_d(r(t),t) = Q_c + Q_s, \qquad (3.2)$$

where

$$D = \frac{C}{3(\mu_a + (1-g)\mu_s)}. \qquad (3.3)$$

Constant D is called the diffusion parameter. C is the speed of light in the medium. $\Phi_d(r(t),t)$ is the average photon flux density (particles per second per unit area, also called the fluence) [24] [23],

$$\Phi_d(r(t),t) = \int_{(4\pi)} I(r(t),\hat{s},t)d\Omega. \tag{3.4}$$

Q_c and Q_s are the coherence field and the local source respectively. The DE equation is a PDE that not always easily solvable. In the DE scattering can have any direction. A simpler model so-called Kubelka-Munk considers only two scattering directions, i.e. forward and backward scattering.

3.1.3 Kubeka-Munk Equations

The Kubelka-Munk (K-M) equations describe the propagation of light in a planar, homogeneous medium, that is illuminated from one side with monochromatic light [23]. The Kubelka-Munk equations are given by [23],

$$-\frac{di}{dx} = -(S+K)i + Sj, \tag{3.5}$$

$$\frac{dj}{dx} = -(S+K)j + Si, \tag{3.6}$$

where x is the depth in the medium and i and j are the intensities of light propagating in the forward and backward directions inside the medium, respectively. S and K are the scattering and absorption per unit thickness, respectively. A general solution of Eq. 3.5 and Eq. 3.6 is given by [23],

$$i = Asinh(bSx) - Bcosh(bSx), \tag{3.7}$$

$$i = (aA - bB)sinh(bSx) - (aB - bA)cosh(bSx), \tag{3.8}$$

where,

$$a = 1 + \frac{K}{S}, \tag{3.9}$$

$$b = (a^2 - 1)^{1/2}. \tag{3.10}$$

Constants A and B can be calculated according to the following conditions,

$$i = I_0 T; j = 0 \text{ for } x=0, \tag{3.11}$$

$$i = I_0; j = I_0 R \text{ for } x=X, \tag{3.12}$$

where the transmittance T and reflectance R are given by,

$$T = b(a \times \sinh(bSX) + b \times (\cosh(bSX))^{-1}, \tag{3.13}$$

$$R = \sinh(bSX)\,(a \times \sinh(bSX) + b \times (\cosh(bSX))^{-1}, \tag{3.14}$$

where X is the full thickness of the medium. It is to be noted that in the K-M model, in addition to considering single backscattered radiation, multiple backscattered radiation is also included.

3.1.4 Beer-Lambert Equations

The simplest method to model light interaction with a single layer of tissue is the Beer-Lambert equation given by [25],

$$\mathrm{I(d)} = (1 - \mathrm{R_F})\mathrm{I_0}\exp(-\mu_t \mathrm{d}), \tag{3.15}$$

where $I(d)$ is the intensity of the light at depth d, R_F is the Fresnel reflection coefficient at the boundary between the tissue and the ambient medium, $\mu_t = \mu_s + \mu_a$ is the extinction coefficient, and I_0 is the incident light intensity.

3.1.5 Monte Carlo simulation of light propagation in turbid media

As mentioned above, analytical solutions of the RTE are only known for restricted simple cases. Hence RTE is usually solved by numerical approaches such as discrete-ordinate method [26], finite-difference method [27] or finite-elements method [28]. Another approach to solve the RTE is based on Monte Carlo methods. A Monte Carlo method can be used as either a numerical quadrature to estimate the value of a definite integral, or as a method to simulate and obtain values of a physical phenomenon. Both Monte Carlo as quadrature [29] [30] and Monte Carlo as simulation [31] have been used for solving the RTE.

3.2 Particle based modeling of the optical properties of tissue

Most biological tissues are turbid media which exhibit strong scattering and low absorption behavior in the presence of light. Their inhomogeneity is due to their constituent components such as cells, fiber structure and organelles [32].

To model such tissues, two approaches have been proposed. The first approach described a single cell of tissue as a collection of microspheres and micro ellipsoids embedded in a finite background medium. This modeling approach is suited to solving Maxwell's equations inside single cells [33]. The second approach models a larger volume of tissue with an ensemble of optically homogeneous particles uniformly suspended in an optically homogeneous background [34]. In this approach the particles can have any shapes or

sizes. However it has been shown that optical properties of randomly oriented particles can be modeled with spherical particles [35]. The choice of spheres for the shape of particles allows analytical calculation of optical coefficients by Mie theory for electromagnetic [36] or scalar wave scattering from spheres [37]. The following subsections discuss the calculation of optical coefficients of tissues modeled with spherical particles inside a homogeneous background.

3.2.1 Refractive Index

The optical coefficients of tissue depend on the refractive-index of its homogeneous background, the refractive index of its particles and their sizes and concentrations. The refractive-index of background, $\bar{n}$, can be calculated by Gladstone-Dale equation [38]:

$$\bar{n} = \sum_{i=1}^{L} n_i f_i, \tag{3.16}$$

where L is the number of tissue components, and f_i is the volume fraction of a particular tissue component, i, in which $\sum_{i=1}^{L} f_i = 1$. Therefore the refractive index of the background medium for soft tissue can be calculated as the weighted average of the refractive index of cytoplasm n_{cp} and the interstitial fluid n_{is},

$$\bar{n}_{bkg} = f_{cp} n_{cp} + (1 - f_{cp}) n_{is}, \tag{3.17}$$

where f_{cp} is the volume fraction of the fluid inside tissue cells [32]. Approximately 60% of the total fluid in a human soft tissue is contained in the intracellular compartment (cytoplasm) and 40% occupies the extracellular compartment (interstitial fluid) [32]. The refractive index of cytoplasm n_{cp}, is typically between 1.35–1.38 [39]. The refractive index of the interstitial fluid n_{is}, is typically between 1.33-1.35 [40]. Assuming $n_{cp} =$

1.37 and $n_{is} = 1.35$ and $f_{cp} = 0.7$ refractive index of the background medium would be $\bar{n}_{bkg} \cong 1.36$ [32].

The refractive index of particles, $\bar{n}_p$, can be modeled as the sum of the refractive index of the background, $\bar{n}_{bkg}$, and the mean of the variation of the refractive indices of cell components, $\overline{\Delta n}$, [32],

$$\bar{n}_p = \bar{n}_{bkg} + \overline{\Delta n}. \tag{3.18}$$

$\overline{\Delta n}$ can be calculated as the weighted average of differences between the refractive index of the cell components and their local background [32],

$$\overline{\Delta n} = f_f(n_f - n_{is}) + f_{nc}(n_{nc} - n_{cp}) + f_{0r}(n_{0r} - n_{cp}), \tag{3.19}$$

where, $n_f, n_{is}, n_{nc}, n_{cp}$ and n_{or} are the refractive indices of cell fiber, interstitial fluid, nuclei, cytoplasm and organelles, respectively. f_f, f_{nc} and f_{or} are the volume fraction of fiber, nuclei and organelles in the solid portion of the tissue. The refractive index of nuclei is reported to be in the narrow range of 1.38–1.41. Assuming the approximation, $n_{or} = n_{nc} = 1.39$, Eq. 3.19 can be simplified into [32],

$$\overline{\Delta n} = f_f(n_f - n_{is}) + (1 - f_f)(n_{nc} - n_{cp}). \tag{3.20}$$

Fibrous-tissue fraction, f_f, depends on the type of tissue. f_f is 0.7 in the dermis, 0.45 for the heart and between 0.02–0.03 for the non-muscular internal organs [34]. Therefore, f_f can vary between the range 0.02-0.7 for different type of tissues which will result in the variation range of 0.03-0.09 for the mean variation of the refractive index, $\overline{\Delta n}$.

3.2.2 Probability distribution of spherical particles sizes

To calculate the optical coefficients, the probability distribution of the particle sizes is needed. It has been shown that the size distribution of particles can be approximated by a skewed log-normal distribution with parameter m,

$$f(x) = C_m x^m \exp\left[-\frac{(\ln x - \ln x_m)^2}{2{\sigma_m}^2}\right], \tag{3.21}$$

where C_m, x_m and ${\sigma_m}^2$ are the normalizing constant, mean and variance of the distribution, respectively. The following unnormalized distribution has been proposed for the volume fraction of particles with radius *r* by rewriting Eq. 3.21[34] ,

$$\eta(r) = \frac{F_v}{C_m}(2r)^{3-D_f} \exp\left[-\frac{(\ln[2r] - \ln[2r_m])^2}{2{\sigma_m}^2}\right]. \tag{3.22}$$

The parameter D_f is so-called the fractal dimension. The normalizing factor C_m is given by,

$$C_m = \sigma_m\sqrt{2\pi}(2r_m)^{4-D_f} \exp\left[\frac{\left(4-D_f\right)^2{\sigma_m}^2}{2}\right]. \tag{3.23}$$

Parameter F_v is the total volume fraction of particles,

$$F_v = \int_0^\infty \eta(r)\,\mathrm{d}r. \tag{3.24}$$

d_m is the mean of the particle size distribution. In the extreme case of infinite broad particle size distribution, this distribution turns into the ideal fractal distribution,

$$\lim_{\sigma_m\to\infty} \eta(r) \approx (2r)^{3-D_f}. \tag{3.25}$$

3.2.3 Optical Coefficients of Particle Based Tissue model

Having calculated the refractive indices and particle size distribution, one can calculate the optical coefficients of tissue.

3.2.3.1 Absorption Coefficient

The absorption coefficient of tissue can be due to absorption in a dispersive background media given by [35],

$$\mu_{a_{bkg}} = \frac{4\pi I(n_{bkg})}{\lambda}, \tag{3.26}$$

where λ is the wavelength of the light and $\mathrm{I}(\mathrm{n_{bkg}})$ is the imaginary part of the refractive index of the background medium. This absorption has non-zero value for any dispersive medium. In tissue modeling this kind of absorption in the background medium is usually neglected. Another cause of light absorption is due to the absorption in the particles. The absorption coefficient of tissue due to the particles with a continuous distribution of particle size is [35],

$$\mu_a = N \int_0^\infty \sigma_{abs}(r) f(r) dr, \tag{3.27}$$

where N and $f(r)$ are the particle concentration and the probability distribution of particles with radius r. $Nf(r)dr$ is the concentration of particles with radii in an interval $(r, r + dr)$ and $\sigma_{abs}(r)$ is the absorption cross-section of particle with radius r.

In the case of particles with M discrete sizes, the absorption coefficient is given by [34],

$$\mu_a = \sum_{i=1}^{M} \mu_a(r_i), \tag{3.28}$$

where $\mu_a(r_i)$ is the absorption coefficient due to particles with radius r_i,

$$\mu_a(r_i) = \frac{\eta(r_i)}{v_i} \sigma_{abs}(r_i), \tag{3.29}$$

where $\sigma_{abs}(d_i)$ and v_i are the absorption cross-section and the volume of a particle with radius r_i and $\eta(d_i)$ is the volume fraction of particles with radius r.

3.2.3.2 Scattering Coefficient

A key assumption in modeling the scattering of light waves in tissue is that scattered optical fields from different particles are independent of each other. The scattering coefficient of tissue modeled with continuous distribution of particle sizes is [35],

$$\mu_s = N \int_0^\infty \sigma_{sca}(r) f(r) dr, \tag{3.30}$$

where $\sigma_{sca}(r)$ is the scattering cross-section of a particle with radius r. In the case of particles with M discrete sizes, the scattering coefficient would be [34],

$$\mu_s = \sum_{i=1}^{M} \mu_s(r_i), \tag{3.31}$$

where $\mu_s(r_i)$ is the scattering coefficient of particles with radius r_i,

$$\mu_s(r_i) = \frac{\eta(r_i)}{v_i} \sigma_{sca}(r_i), \tag{3.32}$$

where $\sigma_{sca}(r_i)$ is the scattering cross-section of a particle with radius r_i.

3.2.3.3 Phase function

The phase function, $P(\hat{S}, \hat{S}')$, is the distribution of the intensity of scattered light in the direction $\hat{S}'$, if the incoming light has direction S. It is assumed that the tissue to be modeled is not birefringent, i.e., its refractive index does not depend on the direction of incoming light. Therefore the phase function of tissue, based on a spherical particles model, can be written as a function of an azimuthal angle, $0 \leq \phi < 2\pi$, and a longitudinal angle, $0 \leq \theta < \pi$,

$$P(\theta, \phi) = P_\Theta(\theta).P_\Phi(\phi), \tag{3.33}$$

where $P_\Theta(\theta)$ and $P_\Phi(\phi)$ are the longitudinal angle and azimuthal angle parts of the scattered intensity distribution. Tissue modeled with spherical particles $P_\Phi(\phi)$ has a uniform distribution in the interval $[0,2\pi]$. The longitudinal part of the phase function of

tissue modeled with an ensemble of particles with continuous range of sizes is given by [35],

$$P_{\Theta}(\theta) = \frac{N\int_0^{\infty} p_{\Theta}(\theta,r)\sigma_{sca}(r)f(r)dr,}{N\int_0^{\infty} \sigma_{sca}(r)f(r)dr}, \tag{3.34}$$

where $p_{\Theta}(\theta, r)$ is the longitudinal scattering phase function of a particle with radius r. In the case of particles with M discrete sizes [35],

$$P_{\Theta}(\theta) = \frac{\sum_{i=1}^{M} \mu_s(r_i)p_{\Theta}(r_i,\theta)}{\sum_{i=1}^{M} \mu_s(r_i)}. \tag{3.35}$$

The anisotropy factor g is defined as the average of the longitudinal scattering angle. In the tissue modeled with discrete particle sizes, g is given by [34],

$$g = \frac{\sum_{i=1}^{M} \mu_s(r_i)g_i(r_i)}{\sum_{i=1}^{M} \mu_s(r_i)}, \tag{3.36}$$

where $g_i(r_i)$ is the anisotropy factor of particles with radius r_i,

$$g_i(r_i) = \int_0^{\pi} \theta\, P_{\Theta}(r_i, \theta)d\theta. \tag{3.37}$$

3.2.3.4 Henyey-Greenstein phase function

Due to the computational complexity of using the phase function defined in Eq. 3.34 and Eq. 3.35, for Monte Carlo simulations, Henyey and Greenstein proposed as an approximation of it. This phase function is commonly used in Monte Carlo simulation of light propagation in tissues [41]. The azimuthal part of the Henyey-Greenstein scattering phase function is uniform,

$$p_{\Phi}^{HG}(\phi) = \frac{1}{2\pi}, 0 \leq \phi < 2\pi. \tag{3.38}$$

The longitudinal part of Henyey-Greenstein phase function, as a function of direction cosine of longitudinal angle, is give by,

$$p^{HG}_{\cos\Theta}(\cos\theta) = \frac{1-g^2}{2(1+g^2-2g\cos\theta_s)^{3/2}}. \quad (3.39)$$

Where g is a given anisotropy factor which is typically about 0.9 for tissues.

3.2.3.5 Packing Factor

As mentioned, all the above equations for optical coefficients are only valid under the assumption that scattered optical fields from different particles are independent of each other. Particles with high sizes or high total volume fraction can violate this assumption. To account for such cases, Twersky proposed a packing factor W [42] [34],

$$W = \frac{(1-F_v)^4}{(1+2F_v)^2}. \quad (3.40)$$

Bascom and Cobbold proposed a modification to this packing factor for particles with arbitrary shape and volume fraction η [43],

$$W_p(\eta) = \frac{(1-\eta)^{p+1}}{[1+\eta(p-1)]^{p-1}}, \quad (3.41)$$

where p is a shape dependent constant called the packing factor. For the spherical particles p=3. To account for the inter-particles correlated scatterings, the modified volume fraction of the particles, $\eta'(r)$, should be used instead of volume fraction $\eta(r)$ in calculation of optical coefficients,

$$\eta'(r) = \frac{(1-\eta(r))^{p+1}}{[1+h(\eta(r)-1)]^{p-1}}. \quad (3.42)$$

3.2.4 Optical cross-sections and phase function of spherical particles

The scattering of the electromagnetic wave from a sphere is known as the Mie theory of scattering. In this research light is modeled as scalar waves. Let the relative refractive index of the sphere to the background be n_r, i.e.,

$$n_p = n_r n_{bkg}. \tag{3.43}$$

It is shown [37] that the scattering cross-section, $\sigma_{sca}(r)$, of a sphere with radius r with relative refractive index n_r, is,

$$\sigma_{sca}(r) = \frac{\pi}{k^2}\sum_{l=0}^{\infty}(2l+1)[1 - 2\eta_l \cos(2\delta_l) + {\eta_l}^2], \tag{3.44}$$

where k is the wavenumber of the planar incident wave. Constants η_l and δ_l is given by,

$$S_l = \eta_l e_l^{i2\delta_l}, 0 \le \eta_l \le 1, \tag{3.45}$$

where S_l is the complex phase shifts given by,

$$S_l \equiv \frac{A_l}{B_l} = -\frac{h_l^{(2)}(\beta)}{h_l^{(1)}(\beta)}\frac{\ln' h_l^{(2)}(\beta) - n \ln' j_l(\alpha)}{\ln' h_l^{(1)}(\beta) - n \ln' j_l(\alpha)}. \tag{3.46}$$

$h_l^{(1)}$, $h_l^{(2)}$ and j_l are spherical Hankel functions of first, second kinds and spherical Bessel function of first kind of order l. Constant β is called the size parameter and is given by,

$$\beta = kr. \tag{3.47}$$

Constant α is given by,

$$\alpha = n_r \beta. \tag{3.48}$$

The absorption cross-section of such sphere is given by,

$$\sigma_{abs}(r) = \frac{\pi}{k^2}\sum_{l=0}^{\infty}(2l+1)[1 - {\eta_l}^2]. \tag{3.49}$$

Due to the symmetry in spheres, the azimuthal part of the scattering phase function is uniform,

$$p_\Phi(\phi, r) = \frac{1}{2\pi}, 0 \le \phi < 2\pi. \tag{3.50}$$

The longitudinal angle part of the scattering phase function is given by,

$$p_{\Theta}(\theta, r) = \frac{|f(k,\theta,\beta)|^2}{\sigma_{abs}(r)}, 0 \leq \theta \leq \pi, \tag{3.51}$$

where $f(k, \theta, \beta)$ is the scattering amplitude of sphere with size parameter β at far field given by,

$$f(k, \theta, \beta) = \frac{1}{2ik}\sum_{l=0}^{\infty}(2l + 1)[S_l(\beta) - 1]P_l(\cos\theta), \tag{3.52}$$

where P_l are the Legendre polynomials of order l.

Chapter 4

Layer-based OCT simulators and modeling of arbitrary shaped media

The first Monte Carlo based simulator of TD-OCT was introduced by Smithies *et al.* in 1998 [44]. In this paper, the authors simulated the TD-OCT signals from homogeneous slab media such as a model intralipid and blood. They showed that the TD-OCT signals follow the extinction-single-backscatter model, at shallow optical depths where single scattered photons are dominant [44]. The extinction-single-backscatter models the TD-OCT imaging process as an incoming beam getting continuously and exponentially attenuated according to the total extinction coefficient of the medium [44][45]. They have also showed that at deeper depth where multiple scattered photons are dominated the localization of backscattered photons was lost. They studied the multiple scattering in terms of the spreading of the point spread function (PSF). PSF of an imaging system is typically defined as the response of it to an illumination by a point source.

They also studied the simulation of OCT signals using Gaussian beam source. To simulate the finite beam, the initial transverse positions of photons are sampled randomly according to the intensity distribution of the source. Next, the photons are directed towards the geometrical focus of the beam. This method is so called *geometric-focus* [10]. Geometric-focus method has also been used in Monte Carlo simulation of laser beam propagation in turbid tissues [46].

The other method which has been used for Monte Carlo simulation of Gaussian beam light interaction with turbid media is called *spot-focus* [10]. In this method the initial

position of photons are sampled randomly as in *geometric-focus*, however the direction of the photons are chosen toward a random point within an area in the focal plane of the beam [10].

The third method used for Monte Carlo simulation of finite beam light propagation in turbid media is using convolution as proposed in [48]. In this method the simulation results for a delta beam source are convolved with the finite size input beam to obtain the simulation result. However this method is only applicable if the problem is shift invariant, i.e., the simulation results are the same for different position of the source such as simulation of light propagation or OCT inside a planar multilayered medium.

In [44] the authors assumed a detection using two lenses as illustrated in Figure 4.1. Their probe has an angle α with the medium to be able to measure Doppler shifts. They implemented their detection system with a rejection process. In the rejection process the collected photon must satisfy a number of criteria on the position and their acceptance angle to contribute to OCT signals.

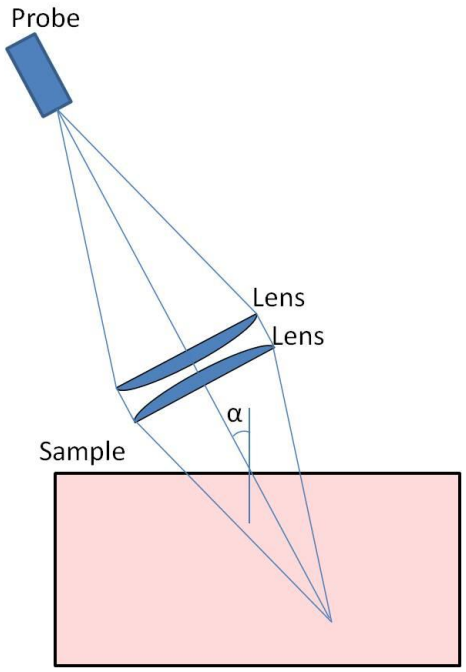

Figure 4.1 Illustration of the detection system used by Smithies *et al* [44].

Tycho *et al.* used a 4F detection system as illustrated in Figure 4.2 [10]. In their 4F detection system the two lenses have equal focal lengths. The probe and the sample are placed in the focal length of their lenses. The distance between two lenses is twice the focal length.

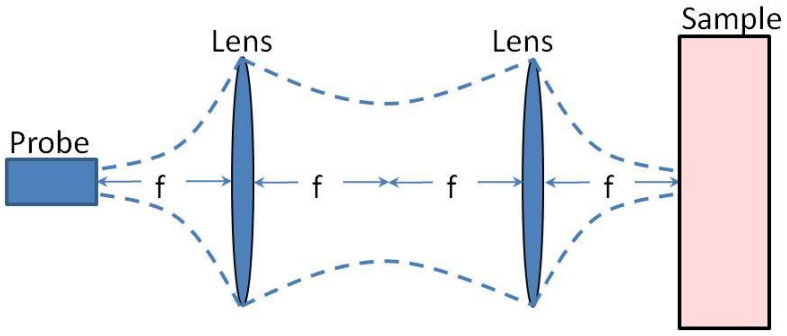

Figure 4.2 The 4F optical system used for detection by Tycho *et al*. [10].

In 1999 Yao and Wang developed a TD-OCT simulator for multilayered media [9]. They introduced Class I and Class II photons as photons backscattered from the target layer in

the medium and photons backscattered from the rest of medium. They showed that these two classes of signal have different spatial and angular distributions [9].

They have also proposed an importance sampling scheme in which they biased the photons travelling away from the probe, towards the inverse of their travelling direction. The detection approach used by Yao and Wang differs from the detection systems in the mentioned OCT simulators. They placed a fiber probe in contact with the media for detection.

Lima *et al.* [13] showed that the importance sampling method by Yao and Wang generated systematic bias resulting in underestimation of TD-OCT signals. They introduce an importance sampling scheme which generates unbiased results and reduces the computation time of calculating Class II diffusive reflectance in TD-OCT by up to three orders of magnitude, comparing with standard Monte Carlo simulation of TD-OCT. Later in 2012 they introduced a simulator with an importance sampling method which reduced the calculation of both Class I and Class II by two orders of magnitudes [14]. The main weakness of these simulators is their restriction to multilayered media. Kirillin *et al.* proposed an OCT simulator of non-planar multilayered objects in which they used different mathematical functions, as opposed to planes, for the boundaries of layers [12]. In [15] they used sinusoidal functions to define the upper and lower boundaries of layers in a model paper.

This method has also been used to simulate the OCT images of the human Enamel [47] in which the boundaries are modeled as non-parallel planes. In [47] Geometric-focus is used to simulate the OCT signals assuming a Gaussian beam source.

This method for modeling non-planar layers has also been used to model human skin in simulation of polarization-sensitive OCT [48].

All of the above OCT simulators are based on a Monte Carlo simulator of light propagation in multilayered media. Recently researchers have attempted to model arbitrary shaped media for simulation of light propagation in turbid tissue. In the next subsection these approaches are briefly discussed.

4.1 Modeling arbitrary shaped media in Monte Carlo simulation of light transportation in tissues.

Monte Carlo simulation of light transport in multilayered turbid media (MCML) was introduced by Wang *et al.* in 1995. The MCML is restricted to multilayer media which limits the applicability of OCT simulators designed based on it.

First efforts to model arbitrary shaped media were cubic voxelization by Pferer *et al.* [49] in which the medium is divided into a number of voxels with different optical properties. This modeling method has been used to simulate the propagation of light in different media such as human brain, skin or trabecular bone [50][51][52].

Another method used to model turbid media is using standard geometrical building blocks such as ellipsoids, cylinders and polyhedrons reported by Li *et al.* [53]. It is used for simulation of bioluminescent light transport in a model mouse which consists of several segmented regions extended from a number of building blocks such as ellipses, cylinders, and polyhedrons.

Cote and Vitkin [54], Margallo-Balbas and French [55] and Ren *et al.* [56] used triangular surface-mesh to model media for simulation of light transport. In this approach the surface of homogeneous regions inside turbid media is modeled by a surface mesh.

Triangular surface-mesh allows approximation of complex tissue structures with any desired accuracy. However, a high computational cost is involved in locating the intersection of the path of a photon with its enclosing surface mesh is the drawback of this method.

To overcome this issue Fang proposed a Plücker coordinate system based mesh-based Monte Carlo method (MMCM) method for fast computation of the location of such intersections [57].

In mesh based approaches, to locate the intersection of the travelling path of photon packets with the enclosing surface mesh, one needs to find intersections with all planes comprising the surface mesh.

If the enclosing surface mesh is convex, the intersection with the minimum distance from the photon's location, among these intersections would be the actual intersection.

Tetrahedrons are convex volumes with minimum number of planes, therefore using them as a building block would minimize the computational cost of simulation.

Most recently Shen and Wang [17] developed tetrahedron-based inhomogeneous Monte-Carlo optical simulator (TIM-OS) where the media is modeled with tetrahedron mesh. My OCT simulator uses the tetrahedron mesh to model the arbitrary media as used in TIM-OS.

Details of different media modeling approaches in simulation of light transport in turbid media can be found in a review paper by Zhu and Liu [58].

Chapter 5 Monte Carlo simulation of OCT for turbid media with arbitrary spatial distribution

To simulate OCT signals of a medium, first one needs to simulate the propagation of light in it. In my simulator the light intensity is represented by photons undergoing a random walk through the medium. The abstract view of operation of this simulator can be seen in Figure 5.1.

The medium consisting of a homogenous background slab and arbitrary shaped homogeneous regions is divided into a number of tetrahedrons. The regions are defined by their optical parameters: scattering coefficient μ_s, absorption coefficient μ_a, refractive index n, and anisotropy factor g.

At the beginning of a simulation a large number of photons are successively launched into the medium. Each photon has a position and travelling direction defined with respect to a rectangular coordinate system placed of the top of the medium with its z-axis normal to the surface of medium as can be seen in Figure 5.1.

During the simulation these photons undergo random walks in the medium. The positions of photons change as they propagate inside the medium. Besides, their travelling directions change due to scatterings, specular reflections or refractions at the boundaries of regions inside the medium. Specular refraction is the change of the travelling direction of photons, when they enter a region with different refractive index. Specular reflection is the reflection of photons at the boundary of regions.

The flowchart of the photons' random walk can be seen in Figure 5.2. In the following subsections I discuss each part of random walk individually in details.

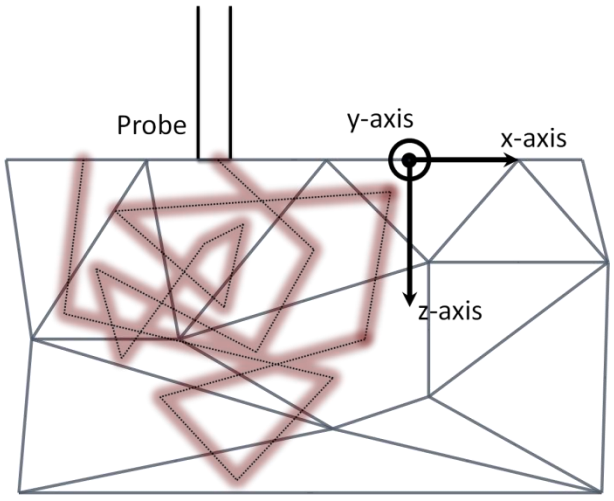

Figure 5.1 An abstract view of the operation of my OCT simulator.

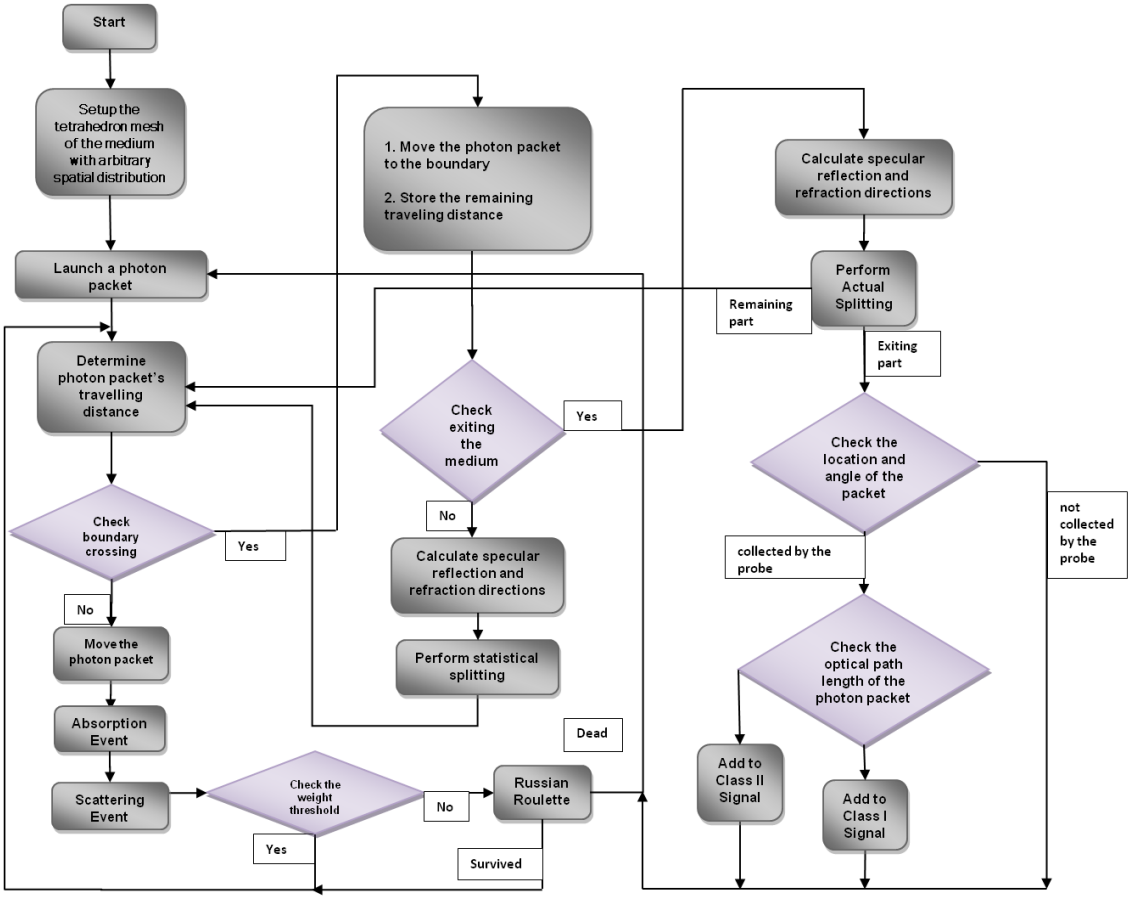

Figure 5.2 The flowchart of photon tracing in my OCT simulator.

5.1 Launching a photon packet

The initial positions of all photons are equal to the light source position to represent the delta beam source. The initial travelling directions of photons are normal to the surface of the medium. Simulations can be performed by tracing one photon by one photon. However, to reduce the simulation time I trace multiple photons grouped in a photon packet at a time by assigning a weight factor, $0 \leq W \leq 1$ to it. This method is proposed by Kahn and Harris to reduce the variance of estimations and computation time in Monte Carlo simulation of particle transmission [59]. The initial weights of photon packets are unity, i.e., $\mathrm{W} = 1$. The weight of the photon packets reduce due to the absorption.

5.2 Determining the photon packet travelling distance

After launching, a photon packet travels a free path after which it undergoes absorption and scattering. The photon packet's free path is the distance that it travels between consequent interactions. The locations that absorption and scattering events happen is so-called the interaction sites.

The cumulative distribution function (CDF), of the free path, S, is given by,

$$P\{S < s\} = 1 - \exp(-\mu_t s), \tag{5.1}$$

where μ_t is the total extinction coefficient of the regions that photon packets travelling in.. The random number generation for my simulator is described in Section 5.3.

After sampling the free path, the photon packets should travel the distance equals to this free path in its travelling direction. However, if the photon packet hits the boundary of the enclosing region during travelling its free path, it will undergo specular reflection and refraction.

5.3 Random number generation

To generate random numbers with specific distributions that are required to simulate OCT signals, I used the following inverse CDF method.

Let $F_X(x) = P\{X < x\}$ be the desired CDF and η be a random variable with a uniform distribution in the interval $[0, 1]$. It can be shown the random variable $Y = {F_X}^{-1}(\eta)$, would have the desired CDF [62]. To generate samples from a specific distribution, samples of a uniformly distributed random variable are transformed using the inverse of the desired CDF.

Hence, one needs to sample a random variable with uniform distribution in the interval $[0, 1]$ first. For this purpose I used a pseudo random number generator (PRNG) that is included in the GNU Scientific Library (GSL) [63], which provides a wide range of PRNGs. I chose to use the PRNG known as *Mersenne Twister* due to its extremely long period of $2^{19937} - 1$ [53] [63]. The *Mersenne Twister* PRNG is a recursive algorithm that starts from a given initial value called the seed. In my OCT simulator, this seed is initialized as,

$$seed = time \,\%\, 10^{15}, \tag{5.2}$$

where $time$ is the number of seconds that passed since midnight, January 1, 1970.

5.4 Photon Hitting a Boundary of Tetrahedron

Photon packets undergo specular reflection and refraction when they enter a region with a different refractive index. Hence, at each step it has to be checked if the photon packet's path and the enclosing tetrahedron intersect. This process is one of the most computationally demanding parts of the simulations.

Let the photon packet position be $\hat{\mathrm{p}}$, its direction $\hat{\mathrm{u}}$, and its free path length s. Therefore any point $\hat{\mathrm{p}}'$on the photon's path satisfies $\hat{p}' = \hat{p} + \hat{u}t$ where $\mathrm{t} \in [0, \mathrm{s}]$. Let $\hat{n}.\hat{u} + d = 0$ be the equation of any plane of the enclosing tetrahedron, where $\hat{\mathrm{x}}$ is any point on this plane, $\hat{\mathrm{n}}$ is its inward normal unit vector and d is its minimum distance from the origin. The distance from the photon's current position to this facet in the direction of photon's travelling direction is given by,

$$\mathrm{t} = -\frac{\hat{\mathrm{n}}.\hat{\mathrm{p}} + \mathrm{d}}{\hat{\mathrm{n}}.\hat{\mathrm{u}}}. \tag{5.3}$$

Let d_b be the minimum positive valued t among four tetrahedron facets. The photon's path and the enclosing tetrahedron intersect if $d_b > s$. If $d_b < s$ the photon remains in the same tetrahedron in which it moves to the interaction site and undergoes absorption and scattering.

If the photon hit the boundary of two tetrahedrons it may undergo specular reflection and refraction if the refractive indices of them differ. Prior to performing the specular reflection and refraction, the photon is moved to the boundary of the two tetrahedrons, i.e.,

$$\hat{p} = \hat{p} + d_b\hat{u}, \tag{5.4}$$

and the remaining of its sampled free photon path, s, is stored in a variable s_{left}, as follows,

$$s_{left} = (s - d_b) \times \mu_t. \tag{5.5}$$

Next the specular reflection and refraction is performed.

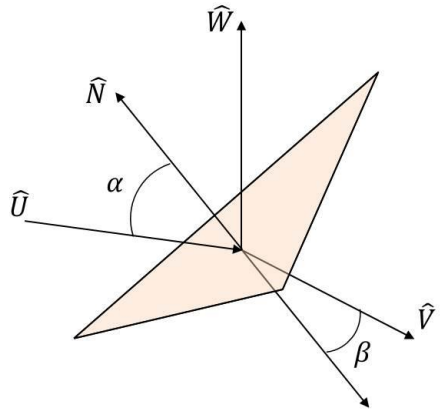

Figure 5.3 Geometrical presentation of vectors and angles involved in reflection and refraction.

5.4.1 Specular reflection and refraction

The geometrical presentation for reflection and refraction can be seen in Figure 5.3. Let the photon packet's direction be $\hat{u}$ and the inward normal vector of the tetrahedron facet which photons hit, be $\hat{n}$. The cosine of the incident angle α is give by,

$$\cos\alpha = |\hat{n}.\hat{u}|. \tag{5.6}$$

The reflection direction $\hat{u}_{reflected}$ is given by,

$$\hat{u}_{reflected} = 2\cos(\alpha)\,\hat{n} + \hat{u}. \tag{5.7}$$

The refraction direction $\hat{u}_{refraction}$ is given by,

$$\hat{u}_{refracted} = \frac{\sin(\beta)}{\sin(\alpha)}(\cos(\alpha)\,\hat{n} + \hat{u}) - \cos(\beta), \tag{5.8}$$

where β is the refraction angle given by the Snell's law,

$$\sin(\beta) = \frac{n_1}{n_2}\sin(\alpha), \tag{5.9}$$

where n_1 is the refractive index of the enclosing tetrahedron and n_2 is the refractive index of the next tetrahedron that the photon packet enters. If α is bigger than the critical angle $\arcsin\left(\frac{n_2}{n_1}\right)$, total internal reflection happens. In total internal reflection the photon

packet is completely reflected from the boundary without refraction. Otherwise portion of photon packet will be reflected with the direction $\hat{u}_{reflected}$ and the rest will be transmitted to the next tetrahedron with the refracted direction $\hat{u}_{refraction}$. Since my code can trace one photon at a time, instead of splitting a photon into two photons I have used statistical splitting. In statistical splitting the photon packet will be reflected with the probability R, or will be refracted with the probability $1-R$. R is the Frensel's coefficient given by,

$$\mathrm{R} = \frac{1}{2}\left(\sin(\alpha)\cos(\beta) - \cos(\alpha)\sin(\beta)\right)^2 \times$$

$$\left[\frac{\left(\cos(\alpha)\cos(\beta) + \sin(\alpha)\sin(\beta)\right)^2 + \left(\cos(\alpha)\cos(\beta) - \sin(\alpha)\sin(\beta)\right)^2}{\left(\sin(\alpha)\cosb(\beta) + \cos(\alpha)\sin(\beta)\right)^2\left(\cos(\alpha)\cos(\beta) + \sin(\alpha)\sin(\beta)\right)^2}\right]. \tag{5.10}$$

If the next region that photon packet enters is the ambient medium, tracing of the refracted part is not needed. Therefore actual splitting can be used. In this case the photon will be reflected with the new weight $W = (1-R)W$ and the refracted part that exits the medium will be stored to check if it contributes to OCT signals.

After performing specular reflection and refraction since the photon has not finished the sampled step size, the remaining part stored in s_{left} calculated according to Eq. 5.5 should be continued. The new step size will be calculated using s_{left} as follows,

$$\mathrm{s} = \frac{\mathrm{S_{left}}}{\mu_t}, \tag{5.11}$$

where μ_t is the extinction coefficient of the enclosing tetrahedron. It can be shown [32] that the CDF of the total step size of the photon through different regions will be,

$$\mathrm{P}\{\mathrm{S} \le \mathrm{s_{sum}}\} = \exp\left(\sum_i \mathrm{s_i}\,\mu_t^i\right), \tag{5.12}$$

where $s_{sum} = \sum_i s_i$ is the total step size and s_i is the step size in the region i with total extinction coefficient μ_t^i.

5.4.2 Photon's Absorption and Scattering

When a photon packet reaches interaction sites it undergoes absorption and scattering. The portion of the photon which will be absorb, ΔW, is given by,

$$\Delta W = W \times \frac{\mu_a}{\mu_t}, \tag{5.13}$$

where μ_a and μ_t are the absorption and extinction coefficient of the enclosing tetrahedron. Therefore the new weight of the photon will be $W = W - \Delta W$.

In scattering events, the photon's direction will change randomly according to the Henyey-Greenstein scattering phase function described in Section 3.2.3.4.

5.4.3 Photon Termination

When a photon packet exits the medium or gets collected by the probe its tracing ends. However, as it propagates in the media, its weight decreases, hence, its effect on the estimates decreases. Therefore, tracing of it can be stopped if its weight falls below a certain threshold. I have used 10^{-4} as the threshold in my simulations. To maintain the unbiased estimation *Russian Roulette* method is used to stop photon packet's tracing. In *Russian Roulette,* a photon packet would be given a chance, with probability $\frac{1}{m}$ to survive or its tracing will be ended with probability $1 - \frac{1}{m}$. If the photon survives, its weight will be increase from W to mW. The constant m is 10 in my simulations.

5.5 Estimation of Class I and Class II OCT signals

The photon packets exiting the media to ambient medium contribute to the OCT signals if they are collected by the probe. Three types of photons collected by the probe constitute the TD-OCT signals; ballistic photons, quasi ballistic photons and multiple scattered photons. Ballistic photons have undergone only a single scattering. Quasi-ballistic photons have undergone multiple scattering within the coherence length of the optical source. Multiple scattered photons have undergone scatterings beyond the coherence length of the optical source.

Ballistic and quasi-ballistic photons are the constituents of Class I diffusive reflectance and the multiple scattered photons are constituents of Class II diffusive reflectance.

Class II diffusive reflectance is the main source of error in OCT imaging and the fundamental limit of OCT imaging depth [45][60].

The probe that I used is a fiber probe as used by Yao and Wang [9] with radius d_{max} and acceptance angle θ_{max}. To classify the photons into Class I and Class II photons I use spatial-temporal indicator functions. Class I diffuse reflectance spatial-temporal indicator function is,

$$I_1(z,i) = \begin{cases} 1, & l_c > |\Delta s_i - 2z_{max}|, r_i < d_{max}, \theta_{z,i} < \theta_{max}, |\Delta s_i - 2z| < l_c \\ 0, & otherwise \end{cases}, \quad (5.14)$$

where l_c is the coherence length of the source, r_i is the distance of the i^{th}- reflected photon packet from the probe, Δs_i is the optical path of i^{th} photon packet, $\theta_{z,i}$ is the angle of the photon packet direction with the z-axis, and z_{max} is the maximum depth reached by the photon packet. Similarly Class II diffuse reflectance, I_2, is,

$$I_2(z,i) = \begin{cases} 1, & l_c < |\Delta s_i - 2z_{max}|, r_i < d_{max}, \theta_{z,i} < \theta_{max}, |\Delta s_i - 2z| < l_c \\ 0, & otherwise \end{cases}. \quad (5.15)$$

Class I diffusive reflectance, $R_1(z)$, and Class II diffusive reflectance, $R_2(z)$, at depth, z, is the weighted mean of these indicator functions,

$$R_{1,2}(z) = \frac{1}{N}\sum_{i=1}^{N} I_{1,2}(z,i)L(i)W(i), \quad (5.16)$$

where N is the number of simulated photon packets, L(i) is a likelihood ratio used in the importance sampling scheme and $W(i)$ is the weight of the i^{th} photon. An estimate of the variance of these estimations is as follows,

$$\sigma^2{}_{1,2}(z) = \frac{1}{N(N-1)}\sum_{i=1}^{N}[I_{1,2}(z,i)L(i)W(i) - R_{1,2}(z)]^2. \quad (5.17)$$

5.6 Importance sampling for reducing computational time of OCT signals

Importance sampling is a name of a family of techniques used to reduce the variance of Monte Carlo estimations using the same number of statistical samples. Therefore, it can be used to reduce the computational cost of a result with a required accuracy. Importance sample can be used in both Monte Carlo as quadrature and Monte Carlo simulations. However, it has to be tailored to each particular estimation.

Typical turbid tissue has a high anisotropy factor, g, hence light most likely propagates in the forward direction inside it. Due to that, the probability of backscattering is very low which will result in the necessity of a very large number of photon to estimate OCT signals. The probability of these back scattering events could be increase by properly biasing the scattering direction..

The importance sampling technique used in this simulator is similar to the one described in [14].

If the travelling direction of the photon is away from the probe ($u_z > 0$), to increase the probability of its detection, it will be biased towards the position of the probe, $\hat{v}$. The geometry of the importance sampling, vectors and angles involved in it can be seen in Figure 5.4.

In the first biased scattering, the following probability density function (PDF) is used to sample the biased longitudinal scattering angle θ_B,

$$p^{B}_{\cos(\Theta)}(\cos\theta_B) = \begin{cases} \left(1 - \frac{1-a}{\sqrt{a^2+1}}\right)^{-1} \frac{a(1-a)}{(1+a^2-2a\cos\theta_B)^{3/2}}, & \cos\theta_B < [0,1] \\ 0, & otherwise \end{cases}, \tag{5.18}$$

where a is the given bias coefficient in the range $[0,1]$.

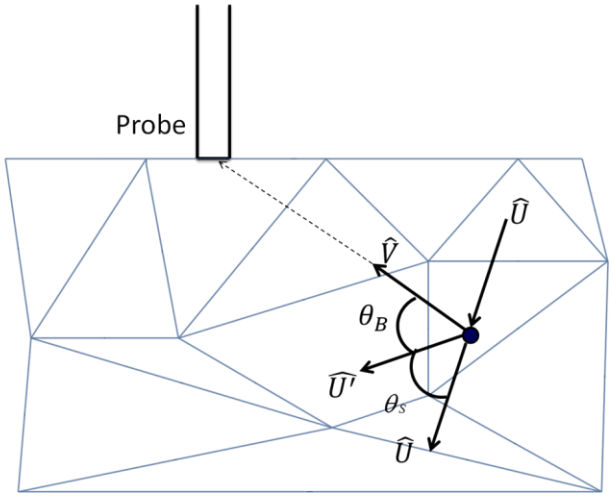

Figure 5.4 Geometry of Importance Sampling method used to reduce the variance of OCT signals estimations.

This process will create biased estimates. To keep the diffusive reflectance estimates unbiased, a compensating likelihood value is assigned to this biased scattering event,

$$L(\cos\theta_B) = \frac{p^{HG}_{\cos(\Theta)}(\cos\theta_s)}{P^{B}_{\cos(\Theta)}(\cos\theta_B)} \tag{5.19}$$

$$= \frac{1-g^2}{2a(1-a)}\left(1-\frac{1-a}{\sqrt{a^2+1}}\right)\left(\frac{1+a^2-2a\cos\theta_B}{1+g^2-2g\cos\theta_s}\right)^{3/2}.$$

After the first biased scattering the photon packet can undergo unbiased scatterings with probability p or other biased scattering with probability $1-p$. In the case of biased scattering the longitudinal scattering angle is sampled from a Henyey-Greenstein phase function that is oriented towards the actual position of the probe with anisotropy factor a. The following likelihood function is assigned for both biased and unbiased scattering events,

$$L(\cos\theta_B) = \frac{p^{HG}_{\cos(\Theta)}(\cos\theta_s)}{p \times P^{B}_{\cos(\Theta)}(\cos\theta_B) + (1-p) \times p^{HG}_{\cos(\Theta)}(\cos\theta_s)}. \tag{5.20}$$

After the tracing of a photon packet ends, due to its collection by the probe, its exit from the medium or being absorbed by it, the total likelihood of the photon packet is calculated. This total likelihood, L, is the product of all likelihood values assigned to all scattering events the photon packet undergone. If $L < 1$, another packet with initial likelihood value of $L' = 1 - L$ will be launched from the previous first scattering event position with a direction sampled from the unbiased Henyey-Greenstein phase function [8].

Chapter 6 Validation and simulation results

I implemented my OCT simulator in ANSI-C. I ran simulations on a 2 GHz Intel Core i7 CPU with 4 GB of RAM.

I validated the simulator by comparing its results to the results obtained from the previously verified OCT simulators by Yao and Wang [9] and Lima *et al.* [14] for a four-layer medium. I have also simulated the OCT signals of a multilayer human skin and compare the results with the results obtained from multilayer OCT simulator by Lima *et al.* [14].

Since importance sampling method used in simulator by Yao and Wang [9] produce underestimated results we used their simulator without the importance sampling, and to obtain results with comparable accuracy we used 10^9 photons.

6.1 Validation of the simulator using a four layer medium

I used a medium consisting of four layers for validation of the simulator, with optical properties, shown in Table 6.1, as used in [31] [13][14]. In all of my simulations the ambient medium is air with refractive index $n = 1$.

To simulate the OCT signals with our novel simulator, we used a tetrahedron mesh with 9600 tetrahedrons and 2205 vertices to represent this four layer medium. We used an optical fiber probe with radius 1 μm, acceptance angle $5°$ and an optical source with coherence length $l_c = 0.015$ mm. We also implemented the importance sampling scheme described above with bias coefficient, $a = 0.925$ and additional bias probability $p = 0.5$. The number of photon used to obtain simulation results in my OCT simulator and

OCT simulator by Lima *et al.* is 10^7. As it is mentioned the importance sampling proposed by Yao and Wang produces underestimated results. Hence I have used their simulator without importance sampling and used 10^9 photons to obtain results with comparable accuracy.

Table 6.1 Optical parameters of the multilayered medium used to validate the new tetrahedron-based OCT simulator.

Layers	Height (cm)	Scattering Coefficient μ_s (cm^{-1})	Absorption Coefficient μ_a (cm^{-1})	Anisotropy Factor g	Refractive Index N
Layer 1	0.0200	60	1.5	0.9	1.0
Layer 2	0.0015	120	3	0.9	1.0
Layer 3	0.0345	60	1.5	0.9	1.0
Layer 4	0.0440	120	3	0.9	1.0

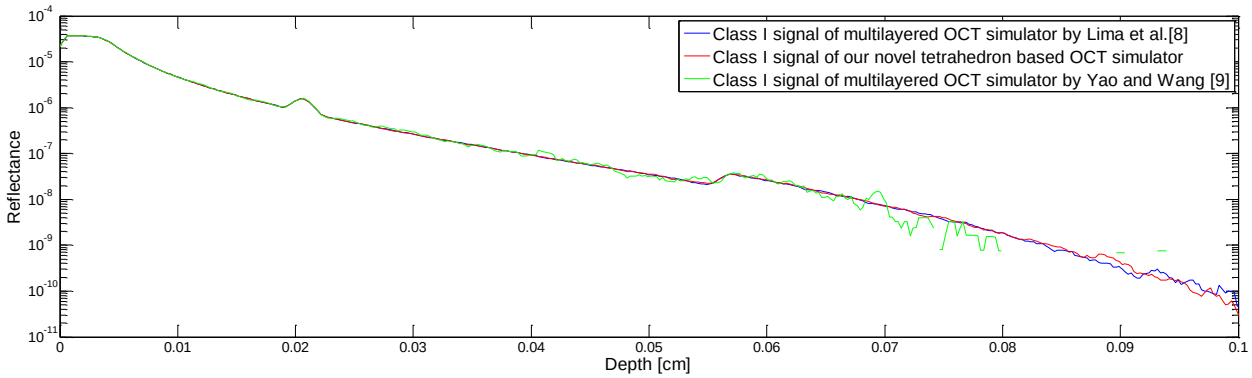

Figure 6.1 Class I diffusive reflectance from the four layer medium described in Table 6.1 at different depth. The green and blue lines are results from the previously validated layered-based OCT simulators by Yao and Wang [9] and Lima *et al.* [14], respectively. The red line represents the Class I signal of my OCT simulator.

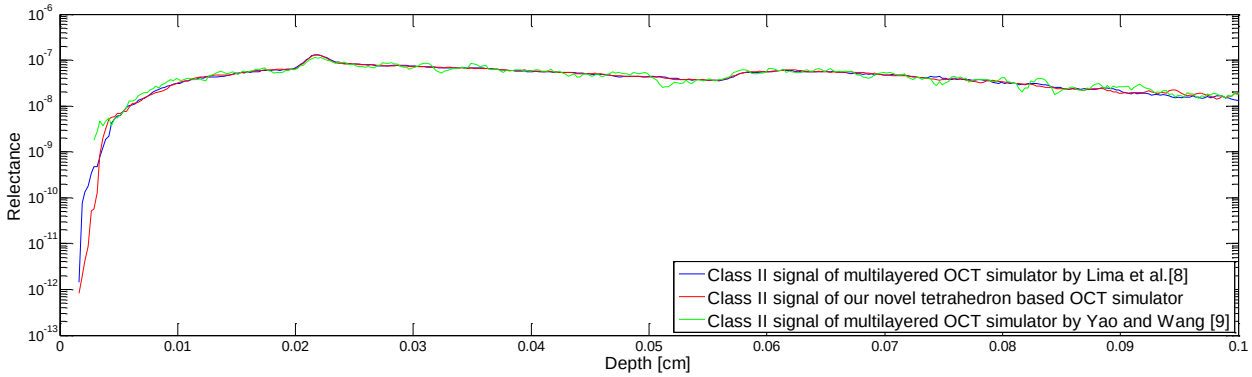

Figure 6.2 Class II diffusive reflectance from the four layer medium described in Table 6.1 at different depth. The green and blue lines are results from the previously validated layered-based OCT simulators by Yao and Wang [9] and Lima *et al.* [14], respectively. The red line represents the Class I signal of our novel tetrahedron based OCT simulator.

Class I and Class II OCT A-scans obtained from the three simulators can be seen in Figure 6.1 and Figure 6.2 respectively. As it can be seen results of the three simulators are in excellent agreement, which validates the results from our new simulator.

The simulation of Class I and Class II diffusive reflectances took 24 minutes on the layer-based simulator by Lima *et al.*[14] on the computer with mentioned specifications. The computation of Class I and Class II diffusive reflectances by my new tetrahedron based simulator took 43 minutes. This is mainly due to the higher computational cost of calculating the intersection of the photon's travelling direction with tetrahedrons in tetrahedron based simulator and photon's travelling direction and infinite planar layers in layered based simulator.

6.2 Validation using a multilayered human skin model.

I have also validated the simulator using a multilayer model of human skin. This model has been used for simulation of light propagation in human skin at wavelength $\lambda = 633$ nm [16]. The optical parameters of this five-layered medium can be seen in Table 6.2.

I used an optical fiber probe with radius 1 μm, acceptance angle 14° and an optical source with coherence length l_c=0.015 mm.

The tetrahedron mesh of this five-layer model has 2646 vertices and 12000 tetrahedrons. The number of photons used is 10^6.

Simulated Class I and Class II OCT A-scan signals obtained from my OCT simulator and the multilayer OCT simulator by Lima *et al.* [14] are shown in Figure 6.3 and Figure 6.4. As it can be seen both Class I and Class II OCT signals obtained from my novel OCT simulator, are in excellent agreement with results obtained from the previously verified layered based OCT simulator [14].

Table 6.2 Optical parameters of five-layered skin model used to validate our OCT simulator.

Layers	*Type*	*Height* (cm)	*Scattering Coefficient* $\mu_s\,(cm^{-1})$	*Absorption Coefficient* $\mu_a\,(cm^{-1})$	*Anisotropy Factor* g	*Refractive Index* n
Layer 1	*Epidermis*	0.01	107	4.3	0.79	1.5
Layer 2	*Dermis*	0.02	187	2.7	0.82	1.4
Layer 3	*Dermis with Plexus Superficialis*	0.02	192	3.3	0.82	1.4
Layer 4	*Dermis*	0.09	187	2.7	0.82	1.4
Layer 5	*Dermis with Plexus Profundus*	0.06	194	3.4	0.82	1.4

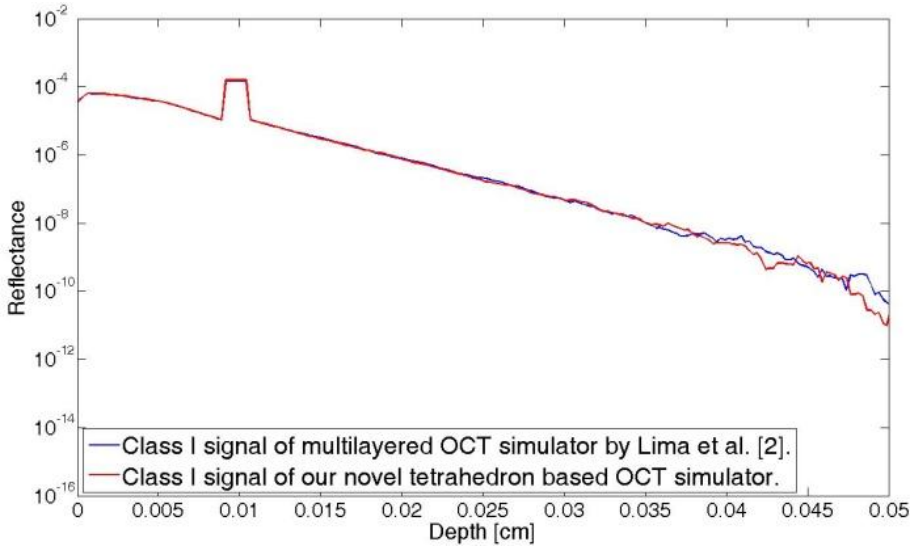

Figure 6.3 A-scan of Class I diffusive reflectance from the five layer human skin model. The blue line is the result from the previously validated layered based OCT simulators by Lima *et al.* [14]. The red line represents the Class I signal of my novel tetrahedron based OCT simulator.

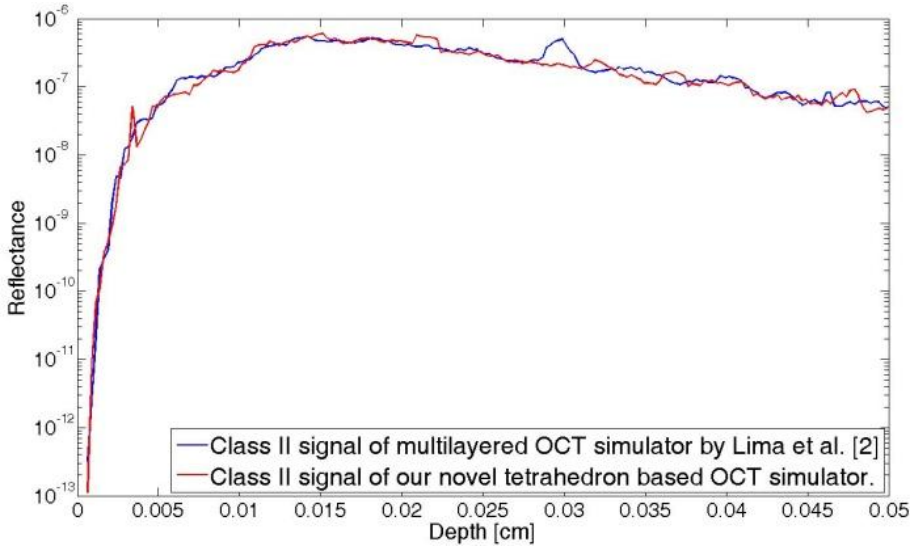

Figure 6.4 A-scan of Class II diffusive reflectance from the five layer human skin model. The blue line is the result from the previously validated layered based OCT simulators by Lima *et al.* [14]. The red line represents the Class I signal of my novel tetrahedron based OCT simulator.

6.3 Simulations of OCT signal from a non-layered objects

In this section, to demonstrate the ability of my new OCT simulator to simulate signals from non-layered objects, the simulated OCT imaging B-Scans of two non-layered media

are presented. First medium is a sphere inside a homogeneous slab and second medium is a homogeneous slab containing an ellipsoid and two spheres.

6.3.1 Simulation of OCT signals from a sphere inside a slab

In the first example of OCT simulation of non-layered objects, I placed a sphere of radius 0.1 mm, at depth 0.2 mm, inside a slab. The slab has 3×3 mm lateral dimensions and 1 mm axial dimension as can be seen in Figure 6.5. The optical properties of this medium can be found in Table 6.3.

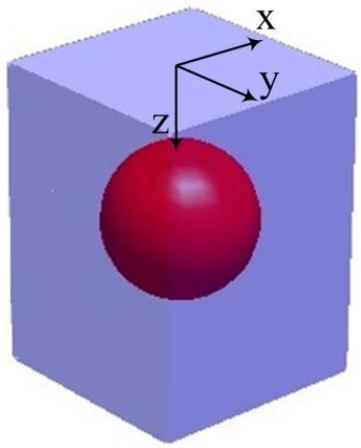

Figure 6.5 Spatial structure of the sphere inside a slab medium.

Table 6.3 Optical parameters of the non-layered medium consisting of a sphere inside a slab.

Medium	Absorption Coefficient $\mu_a\,(cm^{-1})$	Scattering Coefficient $\mu_s\,(cm^{-1})$	Anisotropy Factor g	Refractive Index n
Slab	1.5	60	0.9	1
Sphere	3	120	0.9	1

I used the mesh generator NETGEN [62] to generate the tetrahedron mesh with 4437 tetrahedrons and 800 vertices to represent his medium. I simulated 512 equidistant A-scans along the x-axis from $x = -0.15$ mm to $x = 0.15$ mm to obtain B-scan image of the medium. Tetrahedron mesh and the imaged cross section of the medium are depicted in Figure 6.6.

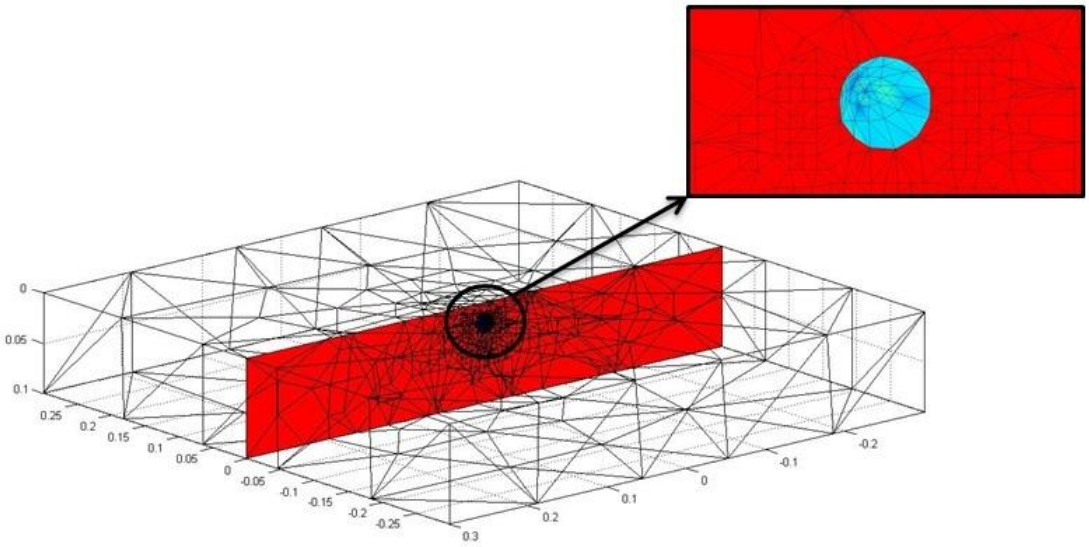

Figure 6.6 The tetrahedron mesh and imaged cross section of the medium consisting of a sphere inside a slab. The black lines in the imaged B-scan cross-section are the intersections of the tetrahedron mesh with the imaged cross-section.

Figure 6.7 shows the simulated B-scan OCT images of this medium which took 360 hours on my computer. As it can be seen in Figure 6.7a, the Class I diffusive reflectance B-scan is remarkably similar to the medium since it is due to the ballistic and quasi ballistic photons. Furthermore, the intensity of Class I image is considerably reduces with depth. This is due to the lower probability of single backscattering from deeper depth and absorption of the medium.

As it can be seen in Figure 6.7b, the intensity of the Class II diffusive reflectance increases with depth since it is due to the multiple scattering photon. However eventually it decreases due to absorption in the medium. Also as it can be seen in Figure 6.7b the Class II signals are particularly stronger inside the sphere, since its scattering coefficient is higher.

All these observations are similar to what is expected from physical OCT imaging, which further validates my new simulator.

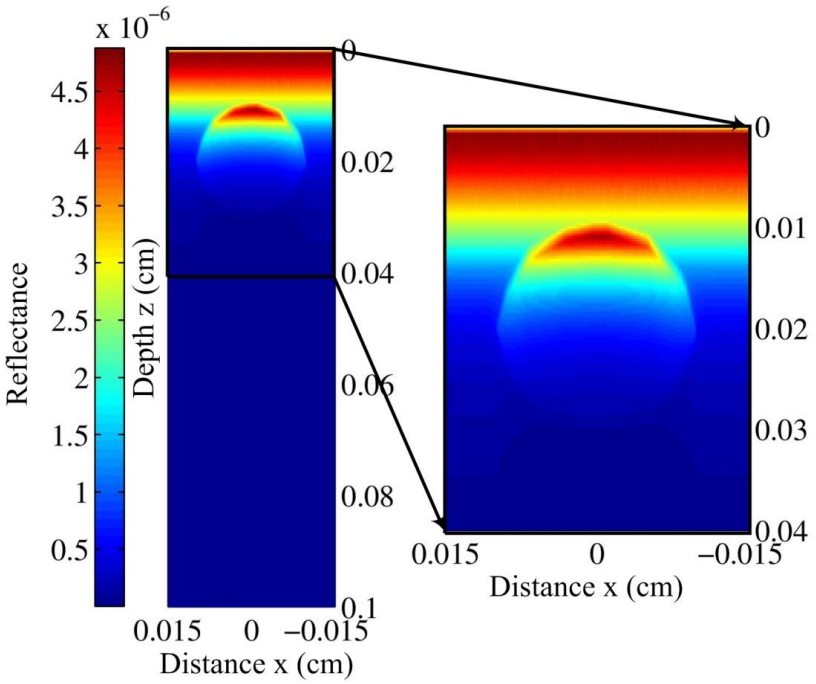

(a)

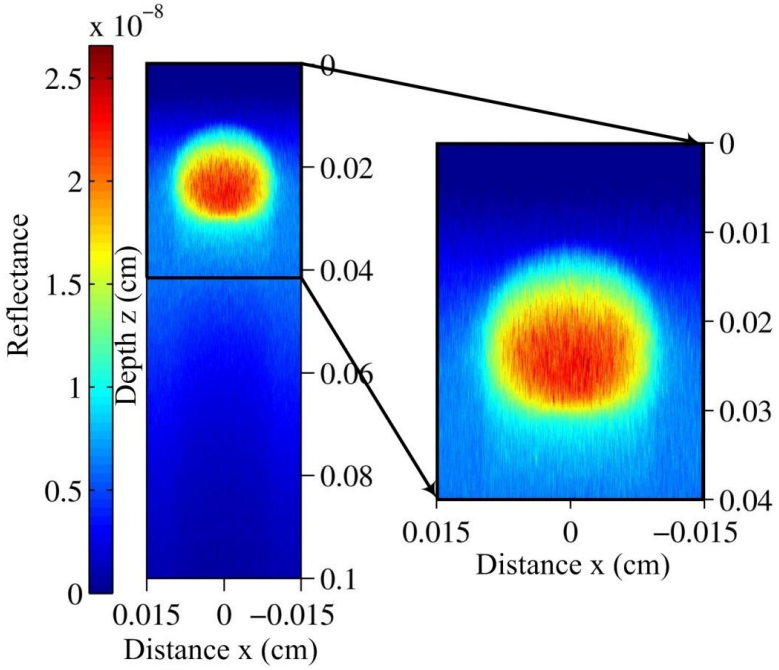

(b)

Figure 6.7 Simulated (a) Class I and (b) Class II reflectance based B-scan OCT image of our non-layered object.

6.4 Resolution, Accuracy and Speed of the Simulator

Three aspects of great importance in the simulator are: (1) resolution, (2) accuracy and (3) computational time.

6.4.1 Resolution of the simulator

As mentioned in chapter 2, in physical OCT systems, the lateral resolution depends of the numerical aperture and the wavelength of the finite beam source. However, in my simulations the source is a delta beam. Therefore, lateral resolution of simulated images is equal to the distance between sequential simulated A-scans.

To illustrate the effect of lateral resolution in the simulated images, I have simulated the OCT images of the above non-layered medium using 75 equidistant A-scans along the x-axis from x = -0.15 mm to x = 0.15 mm. All the parameters of the probe and importance sampling are the same as previously used for simulating 512 A-scans of this object.

Figure 6.8a and Figure 6.8b illustrates the simulation results of Class I and Class II B-Scans respectively.

As it can be seen the lateral resolution is lower however the sphere is still distinguishable. The simulation of these images took approximately 53 hour on my computer which shows linear relationship between the computational time of the simulations and the number of simulated A-Scans. Generally, one should choose the distance between A-Scans; hence the lateral resolution, according to the medium.

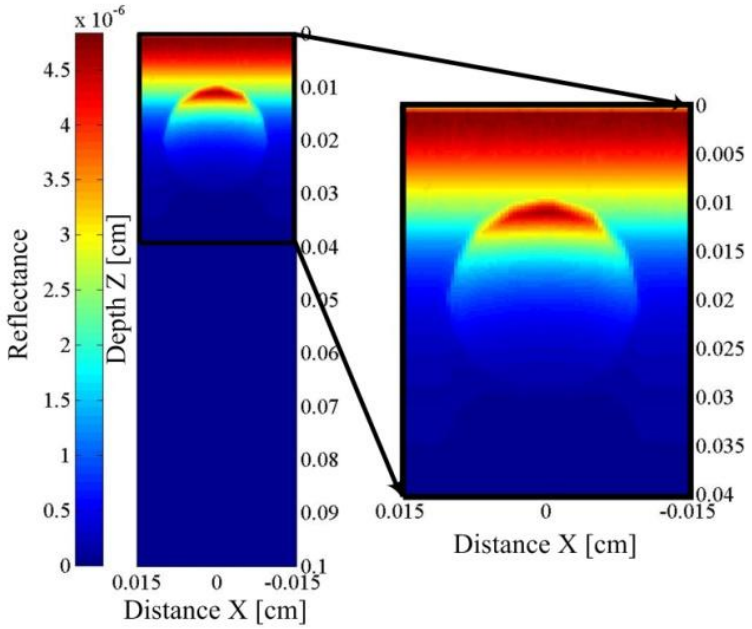

(a)

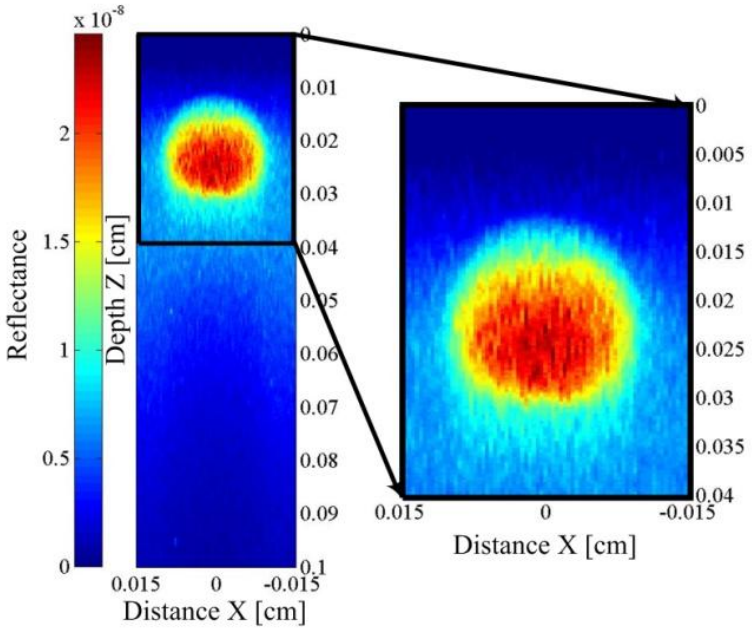

(b)

Figure 6.8 Simulated (a) Class I and (b) Class II reflectance OCT images of the non-layered medium consisting a sphere inside a slab using 75 A-Scans.

As mentioned in chapter 2 the axial resolution of physical OCT systems depends on the coherence length of the source. The simulated axial resolution of my simulator also depends on the coherence length to resemble the physical OCT systems. I divide the depth of media into coherence length intervals similar to the coherence gates in a physical TD-OCT system. Each interval will be presented by a single pixel at its middle point in the B-Scans.

According to Eq. 5.14 and Eq. 5.15 each photon collected by the probe that travelled the optical depth Δs_i will be assigned to the interval with the middle point z such that,

$$|\Delta s_i - 2z| < l_c, \tag{6.1}$$

Then it will be classified as Class I and Class II according to Eq. 5.14 and Eq. 5.15. If the maximum depth the photon reach is z_{max}, it will be classified as Class I or Class II photon if it satisfies the conditions,

$$l_c > |\Delta s_i - 2z_{max}|, \tag{6.2}$$

or,

$$l_c < |\Delta s_i - 2z_{max}|, \tag{6.3}$$

respectively. I have also allowed the simulator to oversample the imaging depth by dividing the intervals into a number of sub-resolution intervals. Therefore, the simulated axial resolution depends of the simulator δz is,

$$\delta z = \frac{l_c}{n_s} \tag{6.4}$$

Where n_s is the number of oversampling. Number of oversampling ratio is 6 in all our simulations.

While smaller coherence length and more oversampling will increase the axial resolution of the simulated images, the computational time of the Monte Carlo simulation remain constant.

6.4.2 Accuracy of the simulator

In general the accuracy of Monte Carlo simulations depends on the variance of the estimations. Figure 6.9 illustrates the Class I signal estimate of an A-scan at x=0 of our non-layered sphere inside a slab medium at different depth along with confidence interval of the estimates using different number of photons.

The confidence interval of Class I and Class II signal estimates, $\mathrm{CI}_{1,2}(z)$, are defined as,

$$\mathrm{CI}_{1,2}(z) \equiv [\mathrm{R}_{1,2}(z) - \sigma_{1,2}(z), \mathrm{R}_{1,2}(z) + \sigma_{1,2}(z)]. \tag{6.5}$$

As it can be seen in Figure 6.9a the confidence interval increases with the depth relative to the signal value. Therefore, we can say that the accuracy of Class I estimates decreases with depth relative to the signal value which is also reported by Yao and Wang [9].

To quantify this fact we use the signal-to-the-computational-noise-ratio, $\mathrm{SNR}_{1,2}(z)$ as another measure of accuracy of our estimated Class I and Class II signals,

$$\mathrm{SNR}_{1,2}(z) = \frac{\mathrm{R}_{1,2}(z)}{\sigma_{1,2}(z)}. \tag{6.6}$$

The signal-to-the-computational-noise-ratio of the Class I signal for different depths, $\mathrm{SNR}_1(z)$, at $x = 0$ of the sphere inside a slab medium can be seen in Figure 6.9b.

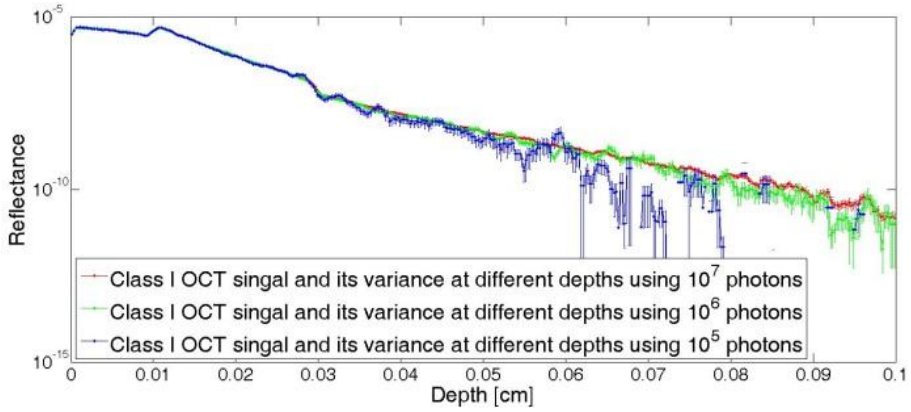
Reflectance
Depth [cm]
Class I OCT singal and its variance at different depths using 10^7 photons
Class I OCT singal and its variance at different depths using 10^6 photons
Class I OCT singal and its variance at different depths using 10^5 photons

(a)

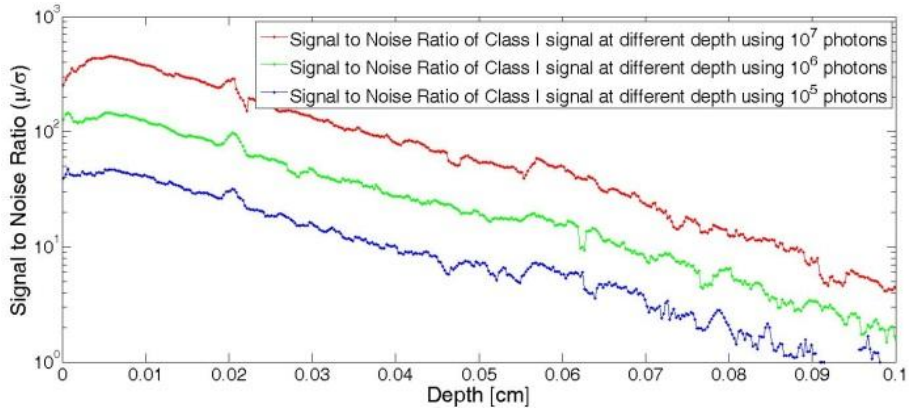
Signal to Noise Ratio (μ/σ)
Depth [cm]
Signal to Noise Ratio of Class I signal at different depth using 10^7 photons
Signal to Noise Ratio of Class I signal at different depth using 10^6 photons
Signal to Noise Ratio of Class I signal at different depth using 10^5 photons

(b)

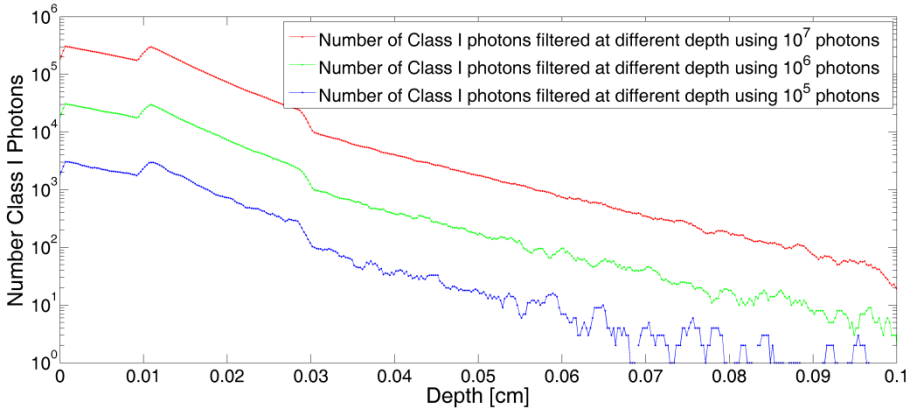
Number Class I Photons
Depth [cm]
Number of Class I photons filtered at different depth using 10^7 photons
Number of Class I photons filtered at different depth using 10^6 photons
Number of Class I photons filtered at different depth using 10^5 photons

(c)

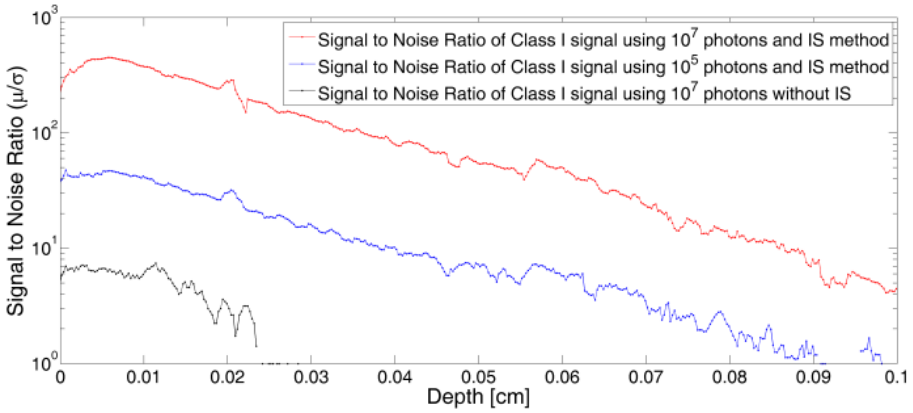

(d)

Figure 6.9 (a) Estimated Class I signal and the confidence intervals at different depth, (b) the signal to the computational noise ratio of the estimated Class I signal, (c) Number of Class I photons filtered at different depth in simulation with different number of photons (d) signal to the computational noise of Class I signal estimates using importance sampling with 10^7 and 10^5 photons and without importance sampling using 10^7 photons.

Signal-to-the-computational-noise of Class I estimate decrease as the depth increases. This fact is due to the lower number of Class I collected photons that backscattered from deeper depth as it can be seen in Figure 6.9c.

The signal to noise ratio is a linear function of the inverse of the square root of the number of photons used in simulations as it can be seen in Figure 6.9b and Figure 6.9c,

$$\mathrm{SNR}_{1,2}(\mathrm{z}) \propto \sqrt{N}, \tag{6.7}$$

which is expected in Monte Carlo simulations. Therefore to increase the accuracy of estimations one should use a large number of photons. However, increasing the number of photons would linearly increase the computational time of simulations.

Finally Figure 6.9d illustrate the effect of our importance sampling technique. In this figure the signal-to-the-computational-noise-ratio of three Class I A-Scans of our sphere inside a slab medium at x=0 is illustrated. Two of the A-Scans are obtained using the

importance sampling technique explained above with 10^7 and 10^5 photons. The third A-Scan is obtained using 10^7 photons, without using importance sampling. Figure 6.9d shows that importance sampling has improved the accuracy of estimations about two orders of magnitude by reducing the variance of estimations.

6.4.3 Computational time of the simulator

To profile the computation time of my simulator, I used a performance analyzer tool that is included in *Microsoft Visual Studio 2013, Ultimate Edition*. Fractions of the total time spent to obtain a typical A-Scan are shown in Figure 6.10.

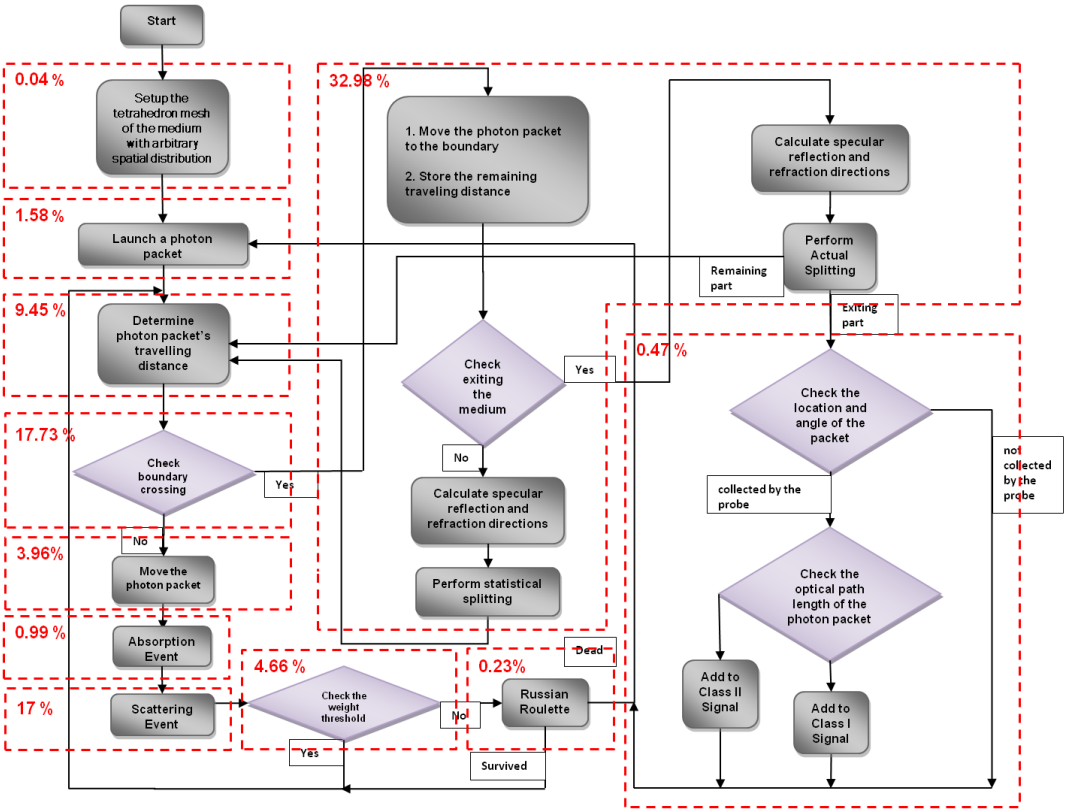

Figure 6.10 Fractions of the total time spent to obtain a typical A-Scan.

Note that the most computationally demanding modules of the simulator are 1) checking intersection of a photon packet's path with its enclosing tetrahedron, and 2) performing

specular reflection and refraction. These profiling results also show that generating the uniformly distributed random samples comprise 22.41% of the total simulation time.

There are a number of options to decrease the computational time of simulations. First is using lower number of A-Scans which reduce the lateral resolution of simulated images. Second is using a lower number of photons which results in lower accuracy of the simulation results. The third method to increase the speed of simulation is parallel implementation of the simulator. Parallel implementation of OCT from multilayered media on Graphics Processor Units (GPU) using Compute Unified Device Architecture **(**CUDA) programming language is described in [63]. Some of parallel implementation of simulation of light transportation in turbid media are [64] [65][66]. Hardware implementation on Field-Programmable Gate Array (FPGA), has also been used to reduce the computational time of simulation of light propagation in turbid media, which can also be a decent candidate to speed up our simulator.

6.5 Simulation of OCT signals from an ellipsoid and two spheres inside a slab

As another example, I have simulated the OCT images of a media consisting of a slab with two spheres and an ellipsoid inside it. The slab is extended for 3 mm in each lateral dimension and 1 mm in the axial direction. The ellipsoid is placed at the position $(0.0\ ,0.0\ ,0.02\ )$. The three vectors defining this ellipsoid, v_1, v_2 and v_3 are,

$$v_1 = [\ 0.006sin(60°), 0, -0.006cos(60°)\ ]^T,$$

$$v_2 = [\ 0\ ,0.1\ ,0\ ]^T$$

$$v_3 = [\ 0.0170sin(30°),\ 0,\ 0.0170cos(30°)\ ]^T.$$

Two spheres have radius $0.005\,mm$ and are placed at positions $(0.008, 0.0, 0.01)$ and $(-0.008, 0.0, 0.03)$. The abstract view of the medium can be seen in Figure 6.11.

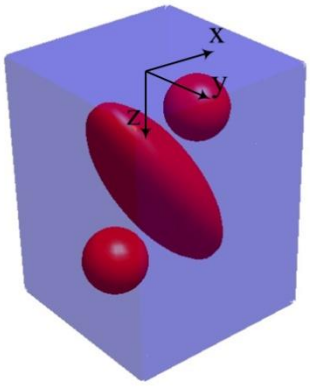

Figure 6.11 Spatial structure of the ellipsoid and two spheres inside a slab medium.

The optical parameters of this medium can be seen in Table 6.4. I used NETGEN [62] to generate the tetrahedron mesh of this medium. The resulting tetrahedron mesh has 5248 vertices and 29697 tetrahedrons. The simulation result of the Class I and Class II OCT B-Scans can be seen in Figure 6.12.

Table 6.4 Optical parameters of the medium consisting of a slab with an ellipsoid and two spheres inside it.

Medium	Absorption Coefficient $\mu_a\ (cm^{-1})$	Scattering Coefficient $\mu_s\ (cm^{-1})$	Anisotropy Factor g	Refractive Index n
Slab	1.5	60	0.9	1
Spheres	3	120	0.9	1
Ellipsoid	3	120	0.9	1

Similar to the previous example, it can be seen in Figure 6.12a the Class I signal decreases with the depth. The ellipsoid and the sphere placed in the lower depth are visible in the Class I B-Scan, however the sphere at the deeper depth is not observable. As it can be seen in Figure 6.12b the boundaries of the regions are mixed in Class II B-scan.

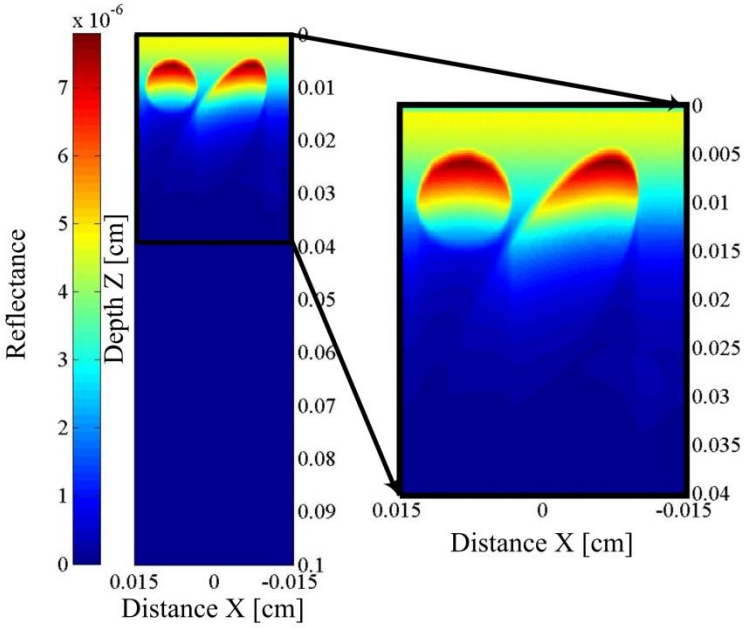

(a)

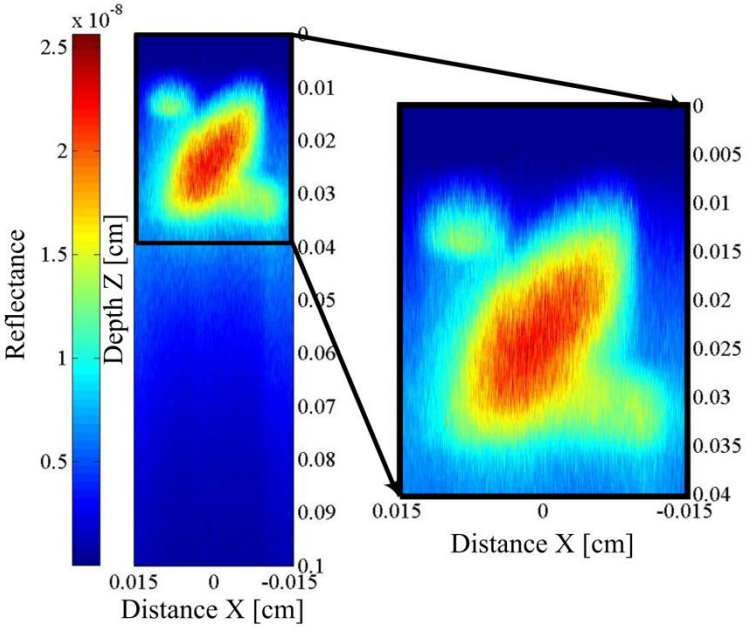

(b)

Figure 6.12 Simulated (a) Class I and (b) Class II reflectance based B-scan OCT images of the medium consisting of a slab with an ellipsoid and two spheres inside it.

Chapter 7

Conclusions and suggested future work

7.1 Conclusions

I have developed a novel Monte Carlo based simulator of OCT imaging for turbid media with arbitrary spatial distributions. This simulator allows computation of both Class I and Class II diffusive reflectance based OCT images. I used a tetrahedron mesh to model media with arbitrary spatial distribution. This tetrahedron-based mesh allows modeling of any arbitrary shaped medium with any desired accuracy. Tetrahedron meshes minimize the computation cost required to obtain the intersection of a photon path with any other surface meshes. I have also implemented an importance sampling to significantly decrease the computational time of simulations by approximately two orders of magnitude.

I have validated the simulator by comparing its results to results from previously validated OCT simulators for a four layer medium and a multi layer model of human skin. I presented simulation results for OCT imaging of two non-layered media, which would not have been possible with earlier simulators. This simulator could be a useful tool to further study OCT and to design new Oct systems with improved performance.

7.2 Suggested future Work

The main drawback of this simulator is its high computational time. Therefore increasing the speed of the simulator is probably the most important goal of any future work based on this thesis. As mentioned in Chapter 5 my simulator successively traces a large number of independent photons. Therefore a parallel implementation of this simulator

can decrease the time of simulation drastically. Hardware implementation of this simulator on FPGA, can also be used to reduce its computational time.

Another potential improvement is to use a finite size optical beam as a more realistic illumination source.

Finally, a SS-OCT simulator could be designed and implemented based on this simulator. Such a SS-OCT simulator would require calculation of the optical coefficients of imaged tissue for different wavelengths. The particle based tissue model described in chapter 2 could be used to calculate these wavelength-dependent optical coefficients.

Bibliography

[1] W. Drexler and J. G. Fujimoto, Optical coherence tomography: technology and applications, New York: Springer, 2008.

[2] D. P. Popescu, C. Flueraru, Y. Mao, S. Chang, J. Disano, S. Sherif and M. G. Sowa, "Optical coherence tomography: fundamental principles, instrumental designs and biomedical applications," *Biophysical Reviews,* vol. 33, pp. 155--169, 2011.

[3] J. Welzel, "Optical coherence tomography in dermatology: a review," *Skin Research and Technology,* vol. 7, no. 1, pp. 1-9, 2001.

[4] M. C. Pierce, J. Strasswimmer, B. H. Park, B. Cense and J. F. de Boer, "Advances in optical coherence tomography imaging for dermatology," *J. Invest. Dermatol.,* vol. 123, no. 3, pp. 458-463, 2004.

[5] W. Drexler, U. Morgner, R. K. Ghanta, F. X. Kartner, J. S. Schuman and J. G. Fujimoto, "Ultrahigh-resolution ophthalmic optical coherence tomography," *Nature medicine,* vol. 7, no. 4, pp. 502-507, 2001.

[6] A. Fercher, C. Hitzenberger, W. Drexler, G. Kamp and H. Sattmann, "In vivo optical coherence tomography.," *American journal of ophthalmology,* vol. 116, no. 1, pp. 113-114, 1993.

[7] J. G. Fujimoto, M. E. Brezinski, G. J. Tearney, S. A. Boppart, B. Bouma, M. R. Hee, J. F. Southern and E. A. Swanson., "Optical biopsy and imaging using optical coherence tomography.," *Nature medicine,* vol. 1, no. 9, pp. 970-972, 1995.

[8] G. J. Fujimoto, "Optical coherence tomography for ultrahigh resolution in vivo imaging," *Nature Biotechnology,* vol. 21, no. 11, pp. 1361 - 1367, 2003.

[9] G. Yao and L. V. Wang, "Monte Carlo simulation of an optical coherence tomography signal in homogeneous turbid media," *Physics in medicine and biology,* vol. 44, no. 9, pp. 2307-2320, 1999.

[10] A. Tycho, T. M. Jorgensen, H. T. Yura and P. E. Andersen, "Derivation of a Monte Carlo method for modeling heterodyne detection in optical coherence tomography systems," *Applied optics,* vol. 41, no. 31, pp. 6676-6691, 2002.

[11] R. K. Wang, "Signal degradation by multiple scattering in optical coherence tomography of

dense tissue: a Monte Carlo study towards optical clearing of biotissues," *Physics in medicine and biology*, vol. 47, no. 13, p. 2281–2299, 2002.

[12] M. Y. Kirillin, A. V. Priezzhev, J. Hast and R. Myllyla, "Monte Carlo simulation of optical clearing of paper in optical coherence tomography," *Quantum Electron,* vol. 36, no. 2, pp. 174-180, 2006.

[13] I. T. Lima, A. Kalra and S. S. Sherif, "importance sampling for Monte Carlo simulation of time-domain optical coherence tomography," *Biomedical Optics Express,* vol. 2, no. 5, pp. 1069-1081, 2011.

[14] I. T. Lima, A. Kalra, H. E. Hernandez-Figueroa and S. S. Sherif, "Fast calculation of multipath diffusive reflectance in optical coherence tomography," *Biomedical Optics Express,* vol. 2, no. 5, pp. 692-700, 2012.

[15] M. Y. Kirillin, E. Alarousu, T. Fabritius, R. Myllyla and A. V. Priezzhev, "Visualization of paper structure by optical coherence tomography: Monte Carlo simulations and experimental study," *Journal of the European Optical Society-Rapid publications,* vol. 2, p. 07031, 2007.

[16] V. Tuchin, "Tissue optics," *SPIE Tutorial Texts in Optical Engineering light Scattering Methods and Instrumentation for Medical Diagnosis, TT38,* 2000.

[17] H. Shen and G. Wang, "A tetrahedron-based inhomogeneous Monte Carlo optical simulator," *Physics in medicine and biology,* vol. 55, no. 4, pp. 947-962, 2010.

[18] J. Pawley, Handbook of biological confocal microscopy, Springer, 2010.

[19] A. G. Podoleanu, "Optical coherence tomography," *The British Journal of Radiology,* vol. 78, no. 935, pp. 976-988, 2005.

[20] S. S. Sherif, C. C. Rosa, C. Flueraru, S. Chang, Y. Mao and A. G. Podoleanu, "Statistics of the depth-scan photocurrent in time-domain optical coherence tomography.," *JOSA A,* pp. 16-20, 2008.

[21] J. A. Izatt and M. A. Choma, "Theory of optical coherence tomography," in *Optical Coherence Tomography,* Springer Berlin Heidelberg, 2008, pp. 47-72.

[22] M. Choma, M. Sarunic, C. Yang and J. Izatt, "Choma, Michael and Sarunic, Marinko and Yang, Changhuei and Izatt, Joseph," *Optics Express,* vol. 11, no. 18, pp. 2183-2189, 2003.

[23] J. Ripoll, "Derivation of the scalar radiative transfer equation from energy conservation of Maxwell's equations in the far field.," *JOSA A,* vol. 28, no. 8, pp. 1765-1775, 2011.

[24] J. Mobley and T. Vo-Dinh, "Optical Properties of Tissue," in *Biomedical Photonics*

Handbook, CRC press Boca Raton, FL, 2003.

[25] B. E. Salah, Introduction to subsurface imaging, Cambridge University Press Cambridge, 2011.

[26] V. V. Tuchin, "Light-Tissue Interactions," in *Biomedical Photonics Handbook*, CRC press Boca Raton, FL, 2003.

[27] Z. Guo and S. Kumar, "Discrete-ordinates solution of short-pulsed laser transport in two-dimensional turbid media," *Applied Optics*, vol. 40, no. 19, pp. 3156-3163, 2001.

[28] A. H. Hielscher, R. E. Alcouffe and R. L. Barbour, "Comparison of finite-difference transport and diffusion calculations for photon migration in homogeneous and heterogeneous tissues," *Physics in Medicine and Biology*, vol. 43, no. 5, pp. 1285-1302, 1998.

[29] S. Arridge, M. Schweiger, M. Hiraoka and D. Delpy, "A finite element approach for modeling photon transport in tissue," *Medical physics*, vol. 20, no. 2, pp. 299-309, 1993.

[30] D. O'Brien, "Accelerated quasi Monte Carlo integration of the radiative transfer equation," *Journal of Quantitative Spectroscopy and Radiative Transfer*, vol. 48, no. 1, pp. 41-59, 1992.

[31] J. Fleck Jr and J. Cummings Jr, "An implicit Monte Carlo scheme for calculating time and frequency dependent nonlinear radiation transport," *Journal of Computational Physics*, vol. 8, no. 3, pp. 313-342, 1971.

[32] L. Wang, S. L. Jacques and L. Zheng, "MCML—Monte Carlo modeling of light transport in multi-layered tissues," *Elsevier*, vol. 47, no. 2, pp. 131-146, 1995.

[33] V. V. Tuchin, L. V. Wang and D. A. Zimnyakov, "Tissue Structure and Optical Models," in *Optical Polarizationin Biomedical Applications*, Springer, 2006, pp. 7-28.

[34] A. Dunn and R. Richards-Kortum, "Three-dimensional computation of light scattering from cells," *IEEE Journal of Selected Topics in Quantum Electronics*, vol. 2, no. 4, pp. 898-905, 1996.

[35] J. Schmitt and A. Knuttel, "Model of optical coherence tomography of heterogeneous tissue," *JOSA A*, vol. 14, no. 6, pp. 1231--1242, 1997.

[36] F. Martelli, S. D. Bianco, A. Ismaelli and G. Zaccanti, Light propagation through biological tissue and other diffusive media: Theory, solutions, and software., SPIE Press, 2010.

[37] C. F. Bohren and D. R. Huffman, Absorption and scattering of light by small particles, John Wiley & Sons, 2008.

[38] W. T. Grandy Jr and W. T. Grandy, Scattering of waves from large spheres, Cambridge University Press, 2005.

[39] R. Barer and S. Joseph, "Refractometry of living cells part I. Basic principles," *Quarterly Journal of Microscopical Science,* vol. 3, no. 32, 1954.

[40] T. Vo-Dinh, Biomedical photonics handbook, CRC press, 2010.

[41] E. A. Genina, A. N. Bashkatov and V. V. Tuchin, "Tissue optical immersion clearing," *Expert review of medical devices,* vol. 7, no. 6, pp. 825-842, 2010.

[42] L. G. Henyey and J. L. Greenstein, "Diffuse radiation in the galaxy.," *The Astrophysical Journal.,* vol. 93, pp. 70-83, 1941.

[43] V. Twersky, "Acoustic bulk parameters in distributions of pair-correlated scatterers," *The Journal of the Acoustical Society of America,* vol. 64, no. 6, pp. 1710-1719, 1978.

[44] P. A. Bascom and R. S. Cobbold, "On a fractal packing approach for understanding ultrasonic backscattering from blood," *The Journal of the Acoustical Society of America,* vol. 98, no. 6, pp. 3040-3049, 1995.

[45] D. J. Smithies, T. Lindmo, Z. Chen, J. S. Nelson and T. E. Milner, "Signal attenuation and localization in optical coherence tomography studied by Monte Carlo simulation," *Physics in Medicine and Biology,* vol. 43, no. 10, pp. 3025-3044, 1998.

[46] M. Yadlowsky, J. Schmitt and R. Bonner, "Multiple scattering in optical coherence microscopy," *Applied optics,* vol. 34, no. 25, pp. 5699-5707, 1995.

[47] Z. Song, K. Dong, X. H. Hu and J. Q. Lu, "Monte Carlo simulation of converging laser beams propagating in biological materials," *Applied optics,* vol. 38, no. 13, pp. 2944-2949, 1999.

[48] L. Wang, S. L. Jacques and L. Zheng, "CONV—convolution for responses to a finite diameter photon beam incident on multi-layered tissues," *Computer methods and programs in biomedicine,* vol. 54, no. 3, pp. 141-150, 1997.

[49] B. Shi, Z. Meng, L. Wang and T. Liu, "Monte Carlo modeling of human tooth optical coherence tomography imaging.," *Journal of Optics,* vol. 15, no. 7, p. 075304, 2013.

[50] I. Meglinski, M. Kirillin, V. Kuzmin and R. Myllyla, "Simulation of polarization-sensitive optical coherence tomography images by a Monte Carlo method," *Optics letters,* vol. 33, no. 14, pp. 1581--1583, 2008.

[51] T. J. Pfefer, J. Kehlet Barton, E. K. Chan, M. G. Ducros, B. S. Sorg, T. E. Milner, J. S.

Nelson and A. J. Welch, "A three-dimensional modular adaptable grid numerical model for light propagation during laser irradiation of skin tissue," *IEEE Journal of Selected Topics in Quantum Electronics,* vol. 2, no. 4, pp. 934-942, 1996.

[52] T. Binzoni, T. Leung, R. Giust, D. Rufenacht and A. Gandjbakhche, "Light transport in tissue by 3D Monte Carlo: influence of boundary voxelization," *Computer methods and programs in biomedicine,* vol. 89, no. 1, pp. 14-23, 2008.

[53] D. Boas, J. Culver, J. Stott and A. Dunn, "Three dimensional Monte Carlo code for photon migration through complex heterogeneous media including the adult human head," *Optics express,* vol. 10, no. 3, pp. 159-170, 2002.

[54] T. Li, H. Gong and Q. Luo, "MCVM: Monte Carlo modeling of photon migration in voxelized media," *Journal of Innovative Optical Health Sciences,* vol. 3, no. 2, pp. 91-102, 2010.

[55] H. Li, J. Tian, F. Zhu, W. Cong, L. V. Wang, E. A. Hoffman and G. Wang, "A mouse optical simulation environment (MOSE) to investigate bioluminescent phenomena in the living mouse with the monte carlo method," *Academic Radiology,* vol. 11, no. 9, pp. 1029-1038, 2004.

[56] D. Cote and I. A. Vitkin, "Robust concentration determination of optically active molecules in turbid media with validated three-dimensional polarization sensitive Monte Carlo calculations," *Optics express,* vol. 3, no. 1, pp. 148-163, 2005.

[57] E. Margallo-Balbs and P. J. French, "Shape based Monte Carlo code for light transport in complex heterogeneous tissues," *Optics express,* pp. 13086-14098, 2007.

[58] N. Ren, J. Liang, X. Qu, J. Li, B. Lu and J. Tian, "GPU-based Monte Carlo simulation for light propagation in complex heterogeneous tissues.," *Optics express,* vol. 18, no. 7, pp. 6811--6823, 2010.

[59] Q. Fang, "Mesh-based Monte Carlo method using fast ray-tracing in Pl{\"u}cker coordinates," *Biomedical optics express,* vol. 1, no. 1, pp. 165-175, 2010.

[60] C. Zhu and Q. Liu, "Review of Monte Carlo modeling of light transport in tissues," *Journal of biomedical optics,* vol. 18, no. 5, pp. 050902-050902, 2013.

[61] H. Kahn and T. E. Harris, "Estimation of particle transmission by random sampling.," *National Bureau of Standards applied mathematics series,* vol. 12, pp. 27-30, 1951.

[62] L. L. Carter and E. D. Cashwell, "Particle-transport simulation with the Monte Carlo

method," *TID-26607, US Enery Research and Development Administration,* 1975.

[63] M. Galassi, J. Davies, J. Theiler, B. Gough and G. Jungman, "Gnu Scientific Library: Reference Manual.," Network Theory Ltd., 2003.

[64] M. Matsumoto and T. Nishimura, "Mersenne twister: a 623-dimensionally equidistributed uniform pseudo-random number generator," *ACM Transactions on Modeling and Computer Simulation (TOMACS),* vol. 8, no. 1, pp. 3-30, 1998.

[65] M. Y. Kirillin, A. V. Priezzhev and R. A. Myllyla, "Role of multiple scattering in formation of OCT skin images," *Quantum Electronics,* vol. 38, no. 6, pp. 570-575, 2008.

[66] J. Schoberl, "NETGEN An advancing front 2D/3D-mesh generator based on abstract rules," *Computing and visualization in science,* vol. 1, no. 1, pp. 41-52, 1997.

[67] A. Kalra, I. T. Lima and S. S. Sherif, "Almost instantaneous Monte Carlo calculation of optical coherence tomography signal using graphic processing unit," in *IEEE Photonics Conference (IPC),* 2013.

[68] E. Alerstam, T. Svensson and S. Andersson-Engels, "Parallel computing with graphics processing units for high-speed Monte Carlo simulation of photon migration," *Journal of biomedical optics,* vol. 13, no. 6, p. 060504, 2008.

[69] Q. Fang and D. A. Boas, "Monte Carlo simulation of photon migration in 3D turbid media accelerated by graphics processing units," *Optics express,* vol. 17, no. 22, pp. 20178-20190, 2009.

[70] T. S. Leung and S. Powell, "Fast Monte Carlo simulations of ultrasound-modulated light using a graphics processing unit," *Journal of biomedical optics,* vol. 15, no. 5, p. 055007, 2010.

[71] W.-F. Cheong and S. A. W. A. J. Prahl, "A review of the optical properties of biological tissues," *IEEE journal of quantum electronics,* pp. 2166--2185, 1990.

[72] P. F. Pereira and S. S. Sherif, "Design of an optimum ultrasound pattern to minimize multiple-scattered light reflected from inhomogeneous tissue," in *Proc. SPIE,* 2012.

[73] M. Kirillin, I. Meglinski, V. Kuzmin, E. Sergeeva and R. Myllyla, "Simulation of optical coherence tomography images by Monte Carlo modeling based on polarization vector approach," *Optics express,* vol. 18, no. 21, pp. 21714--21724, 2010.

[74] Q. Fang and D. A. Boas, "Monte Carlo simulation of photon migration in 3D turbid media accelerated by graphics processing units.," *Optics express,* vol. 17, no. 22, pp. 20178-20190,

2009.